Magnetic Resonance Imaging

18

Magnetic resonance imaging (MRI) (formerly called nuclear magnetic resonance imaging) provides very-high-resolution images without ionizing radiation. There is also the potential for more elaborate imaging, including flow, diffusion, and the signature of particular atomic environments.

Magnetic resonance phenomena are more complicated than x-ray attenuation or photon emission by a radioactive nucleus. MRI depends upon the behavior of atomic nuclei in a magnetic field; in particular, the orientation and motion of the nuclear magnetic moment in the field. The patient is placed in a strong static magnetic field (typically 1–4 T). This is usually provided by a hollow cylindrical (solenoidal) magnet, though some machines use other configurations so that the physician can carry out procedures on the patient while viewing the MRI image. Other coils apply time-varying spatial gradients to the magnetic field, along with radio-frequency signals that cause the magnetization changes described below. Still other coils detect the very weak radio-frequency signals resulting from these changes.

First, we must understand the property that we are measuring. Section 18.1 describes the behavior of a magnetic moment in a static magnetic field, and Sect. 18.2 shows how the nuclear spin is related to the magnetic moment. Section 18.3 introduces the concept of the magnetization vector, which is the magnetic moment per unit volume, while Sect. 18.4 develops the equations of motion for the magnetic moment. In order to describe the motion of the magnetization, it is convenient—in fact, almost essential—to use the rotating coordinate system described in Sect. 18.5.

To make a measurement, the nuclear magnetic moments originally aligned with the static magnetic field are made to rotate or *precess* in a plane perpendicular to the static field, after which the magnetization gradually returns to its original value. This relaxation phenomenon is described in Sect. 18.6. Sections 18.7 and 18.8 describe ways in which the magnetization can be manipulated for measurement.

Imaging techniques are finally introduced in Sect. 18.9. Sections 18.10 and 18.11 describe how chemical shifts and blood flow can affect the image or can themselves be imaged. The last two sections describe functional MRI (fMRI) and diffusion effects.

18.1 Magnetic Moments in an External Magnetic Field

Magnetic resonance imaging detects the magnetic dipoles in the nuclei of atoms in the human body. We saw in Chap. 8 that isolated magnetic monopoles have never been observed (see Eq. 8.8), and that magnetic fields are produced by moving charges or electric currents. In some cases, such as bar magnets, the external field is the same as if there were magnetic charges occurring in pairs or *dipoles*.[1] The strength of a dipole is measured by its *magnetic dipole moment* $\boldsymbol{\mu}$. (In Chap. 8 the magnetic dipole moment was called $\mathbf{m}$ to avoid confusion with μ_0. In this chapter we use $\boldsymbol{\mu}$ to avoid confusion with the quantum number m and to be consistent with the literature in the field.) The magnetic dipole moment is analogous to the electric dipole moment of Chap. 7; however, it is produced by a movement of charge, such as charge moving in a circular path. The units of $\boldsymbol{\mu}$ are J T^{-1} or A m^2. We saw that when a magnetic dipole is placed in a magnetic field as in Fig. 18.1, it is necessary to apply an external torque $\boldsymbol{\tau}_{\text{ext}}$ to keep it in equilibrium. This torque, which is required to cancel the torque exerted by the magnetic field, vanishes if the dipole is aligned with the field. The torque exerted on the dipole by the magnetic field $\mathbf{B}$ is

$$\boldsymbol{\tau} = \boldsymbol{\mu} \times \mathbf{B}. \tag{18.1}$$

(This is Eq. 8.4.)

[1] Dipoles can be arranged so that their fields nearly cancel, giving rise to still-higher-order moments such as the quadrupole moment or the octupole moment (see Chap. 7). A configuration for which the quadrupole moment is important is two magnets in a line arranged as N-S-S-N.

R. K. Hobbie, B. J. Roth, *Intermediate Physics for Medicine and Biology*,
DOI 10.1007/978-3-319-12682-1_18,

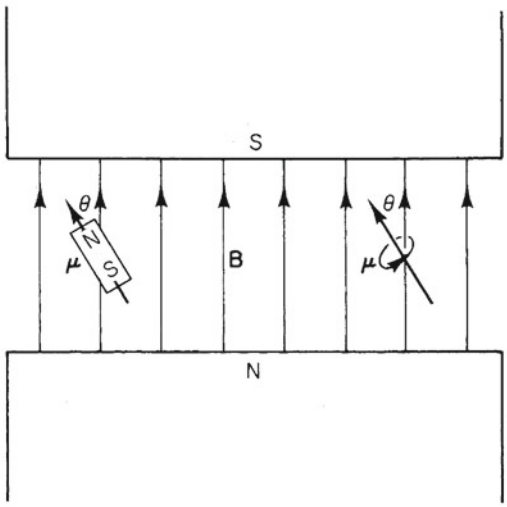

Fig. 18.1 A magnetic dipole in a magnetic field. The dipole can be either a bar magnet or a current loop

The potential energy of the dipole is the work that must be done by $\boldsymbol{\tau}_{\text{ext}}$ to change the dipole's orientation in the magnetic field without changing any kinetic energy it might have. To increase angle θ by an amount $d\theta$ requires that work be done on the dipole-magnetic field system. This work is the increase in potential energy of the system:

$$dU = \mu B \sin\theta \, d\theta. \tag{18.2}$$

This can be integrated to give the change in potential energy when the angle changes from θ_1 to θ_2:

$$U(\theta_2) - U(\theta_1) = -\mu B(\cos\theta_2 - \cos\theta_1).$$

If the energy is considered to be zero when the dipole is at right angles to **B**, then the potential energy is

$$U(\theta) = -\mu B \cos\theta = -\boldsymbol{\mu} \cdot \mathbf{B}. \tag{18.3}$$

In many cases the moving charges that give rise to the magnetic moment of an object possess angular momentum **L**. Often the magnetic moment is parallel to and proportional to the angular momentum: $\boldsymbol{\mu} = \gamma \mathbf{L}$. The proportionality factor γ is called the *gyromagnetic ratio* (sometimes called the magnetogyric ratio). When such an object is placed in a uniform magnetic field, the resulting motion can be quite complicated. The torque on the object is $\boldsymbol{\tau} = \boldsymbol{\mu} \times \mathbf{B} = \gamma \mathbf{L} \times \mathbf{B}$. It is not difficult to show (Problem 1) that the torque is the rate of change of the angular momentum, $\boldsymbol{\tau} = d\mathbf{L}/dt$. Therefore the equation of motion is

$$\gamma(\mathbf{L} \times \mathbf{B}) = \frac{d\mathbf{L}}{dt} \tag{18.4a}$$

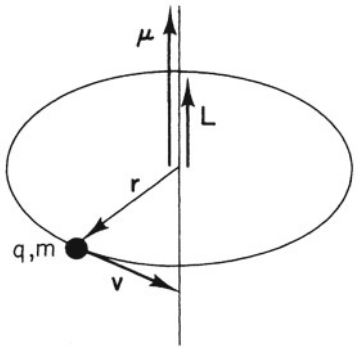

Fig. 18.2 A particle of charge q and mass m travels in a circular orbit. It has a magnetic moment $\boldsymbol{\mu}$ and angular momentum **L**. If the charge is positive, $\boldsymbol{\mu}$ and **L** are parallel; if it is negative they are in opposite directions

or

$$\gamma(\boldsymbol{\mu} \times \mathbf{B}) = \frac{d\boldsymbol{\mu}}{dt}. \tag{18.4b}$$

Solutions to these equations are discussed in Sect. 18.4.

18.2 The Source of the Magnetic Moment

Atomic electrons and the protons and neutrons in the atomic nucleus can possess both angular momentum and a magnetic moment. The magnetic moment of a particle is related to its angular momentum. We can derive this relationship for a charged particle moving in a circular orbit. We saw in Chap. 8 that the magnitude of the magnetic moment of a current loop is the product of the current i and the area of the loop S:

$$|\boldsymbol{\mu}| = \mu = iS. \tag{18.5}$$

The direction of the vector is perpendicular to the plane of the loop. Its direction is defined by a right-hand rule: curl the fingers of your right hand in the direction of current flow and your thumb will point in the direction of $\boldsymbol{\mu}$ (see the right-hand part of Fig. 18.1). This is the same right-hand rule that relates the circular motion of a particle to the direction of its angular momentum.

Suppose that a particle of charge q and mass m moves in a circular orbit of radius r as in Fig. 18.2. The speed is v and the magnitude of the angular momentum is $L = mvr$. The effective current is the charge q multiplied by the number of times it goes past a given point on the circumference of the orbit in one second: $i = qv/2\pi r$. The magnetic moment has magnitude $\mu = iS = i\pi r^2 = qvr/2$. Since the angular momentum is $L = mvr$ and $\boldsymbol{\mu}$ and **L** are both perpendicular

Table 18.1 Values of the spin and gyromagnetic ratio for a free electron and various nuclei of interest

Particle	Spin	$\gamma = \omega_{\text{Larmor}}/B$ ($\text{s}^{-1}\ \text{T}^{-1}$)	ν/B ($\text{MHz}\ \text{T}^{-1}$)
Electron	$\frac{1}{2}$	1.7608×10^{11}	2.8025×10^{4}
Proton	$\frac{1}{2}$	2.6753×10^{8}	42.5781
Neutron	$\frac{1}{2}$	1.8326×10^{8}	29.1667
^{23}Na	$\frac{3}{2}$	0.7076×10^{8}	11.2618
^{31}P	$\frac{1}{2}$	1.0829×10^{8}	17.2349

to the plane of the orbit, we can write

$$\boldsymbol{\mu} = \left(\frac{q}{2m}\right)\mathbf{L} = \gamma\,\mathbf{L}. \tag{18.6}$$

The quantity $\gamma = q/2m$ is the gyromagnetic ratio for this system. The units γ of are $\text{T}^{-1}\ \text{s}^{-1}$ (see Problem 2). The magnetic moment and the orbital angular momentum are parallel for a positive charge and antiparallel for a negative charge.

An electron or a proton also has an intrinsic magnetic moment quite separate from its orbital motion. It is associated with and proportional to the intrinsic or *spin* angular momentum **S** of the particle. We write

$$\boldsymbol{\mu} = \gamma\,\mathbf{S}. \tag{18.7}$$

The value of γ for a spin is *not* equal to $q/2m$.

Two kinds of spin measurements have biological importance. One is associated with electron magnetic moments and the other with the magnetic moments of nuclei. Most neutral atoms in their ground state have no magnetic moment due to the electrons. Exceptions are the transition elements that exhibit paramagnetism. Free radicals, which are often of biological interest, have an unpaired electron and therefore have a magnetic moment. In most cases this magnetic moment is due almost entirely to the spin of the unpaired electron.

Magnetic resonance imaging is based on the magnetic moments of atomic nuclei in the patient. The total angular momentum and magnetic moment of an atomic nucleus are due to the spins of the protons and neutrons, as well as any orbital angular momentum they have inside the nucleus. Table 18.1 lists the spin and gyromagnetic ratio of the electron and some nuclei of biological interest.

If the nuclear angular momentum is **I** with quantum number I, the possible values of the z component of **I** are $m\hbar$, where $m = -I, (-I+1), \ldots, I$. For $I = \frac{1}{2}$, the values are $-1/2$ and $1/2$, while for $I = \frac{3}{2}$ they are $-3/2, -1/2, 1/2$, and $3/2$. The direction of the external magnetic field defines the z axis, and the energy of a spin is given by $-\boldsymbol{\mu}\cdot\mathbf{B} = -\gamma\,\mathbf{I}\cdot\mathbf{B} = -\gamma m\hbar B$. The difference between adjacent energy levels is $\gamma B\hbar$, and the angular frequency of a photon corresponding to that difference is $\omega_{\text{photon}} = \gamma B$.

18.3 The Magnetization

The MR image depends on the *magnetization* of the tissue. The magnetization of a sample, **M**, is the average magnetic moment per unit volume. In the absence of an external magnetic field to align the nuclear spins, the magnetization is zero. As an external magnetic field **B** is applied, the spins tend to align in spite of their thermal motion, and the magnetization increases, proportional at first to the external field. If the external field is strong enough, all of the nuclear magnetic moments are aligned, and the magnetization reaches its saturation value.

We can calculate how the magnetization depends on **B**. Consider a collection of spins of a single nuclear species in an external magnetic field. This might be the hydrogen nuclei (protons) in a sample. The spins do not interact with each other but are in thermal equilibrium with the surroundings, which are at temperature T. We do not consider the mechanism by which they reach thermal equilibrium. Since the magnetization is the average magnetic moment per unit volume, it is the number of spins per unit volume, N, times the average magnetic moment of each spin: $\mathbf{M} = N\,\langle\boldsymbol{\mu}\rangle$.

To obtain the average value of the z component of the magnetic moment, we must consider each possible value of quantum number m. We multiply the value of μ_z corresponding to each value of m by the probability that m has that value. Since the spins are in thermal equilibrium with the surroundings, the probability is proportional to the Boltzmann factor of Chap. 3, $e^{-(U/k_BT)} = e^{\gamma m\hbar B/k_BT}$. The denominator in Eq. 18.8 normalizes the probability:

$$\langle\mu_z\rangle = \frac{\gamma\hbar\sum_{m=-I}^{I} m\,e^{\gamma m\hbar B/k_BT}}{\sum_{m=-I}^{I} e^{\gamma m\hbar B/k_BT}}. \tag{18.8}$$

At room temperature $\gamma I\hbar B/k_BT \ll 1$ (see Problem 4), and it is possible to make the approximation $e^x \approx 1+x$. The sum in the numerator then has two terms:

$$\sum_{m=-I}^{I} m + \frac{\gamma\hbar B}{k_BT}\sum_{m=-I}^{I} m^2.$$

The first sum vanishes. The second is $I(I+1)(2I+1)/3$. The denominator is

$$\sum_{m=-I}^{I} 1 + \frac{\gamma\hbar B}{k_BT}\sum_{m=-I}^{I} m.$$

The first term is $2I+1$; the second vanishes. Therefore we obtain

$$\langle\mu_z\rangle = \frac{\gamma^2\hbar^2 I(I+1)}{3k_BT}B. \tag{18.9}$$

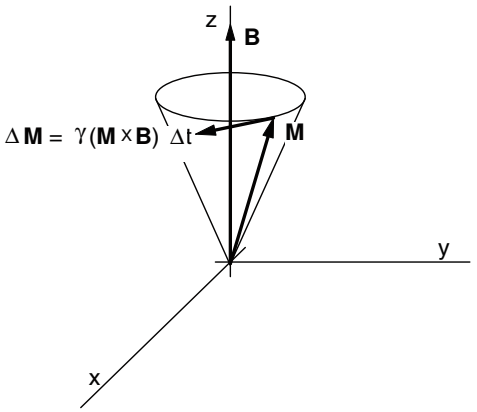

Fig. 18.3 The system with initial magnetization **M** has been given just enough additional angular momentum to precess about the direction of the static magnetic field **B**. The rate of change of **M** is perpendicular to both **M** and **B**. For short time intervals, $\Delta\mathbf{M} = \gamma(\mathbf{M} \times \mathbf{B})\,\Delta t$

The z component of **M** is

$$M_z = N\,\langle\mu_z\rangle = \frac{N\gamma^2\hbar^2 I(I+1)}{3k_B T}B, \tag{18.10}$$

which is proportional to the applied field.

18.4 Behavior of the Magnetization Vector

A remarkable result of quantum mechanics is that the average or expectation value of a spin obeys the classical Eq. 18.4b:

$$\frac{d\,\langle\boldsymbol{\mu}\rangle}{dt} = \gamma\,(\langle\boldsymbol{\mu}\rangle \times \mathbf{B}) \tag{18.11}$$

whether or not **B** is time dependent (Slichter 1990). Multiplying by the number of spins per unit volume we obtain

$$\frac{d\mathbf{M}}{dt} = \gamma\,(\mathbf{M} \times \mathbf{B})\,. \tag{18.12}$$

This equation can lead to many different behaviors of **M**, some of which are quite complicated.

The simplest motion occurs if **M** is parallel to **B**, in which case **M** does not change because there is no torque. Another relatively simple motion, called *precession*, is shown in Fig. 18.3. With the proper initial conditions **M** (and $\langle\boldsymbol{\mu}\rangle$) precess about the direction of **B**. That is, they both rotate about the direction of **B** with a constant angular velocity and at a fixed angle θ with the direction of **B**. Since $\mathbf{M} \times \mathbf{B}$ is always at right angles to **M**, $d\mathbf{M}/dt$ is at right angles to **M**, and the angular momentum does not change magnitude. The analytic solution can be investigated by writing Eq. 18.12 in Cartesian coordinates when **B** is along the z axis:

$$\begin{aligned} \frac{dM_x}{dt} &= \gamma M_y B_z, \\ \frac{dM_y}{dt} &= -\gamma M_x B_z, \\ \frac{dM_z}{dt} &= 0. \end{aligned} \tag{18.13}$$

One possible solution to these equations is

$$\begin{aligned} M_z &= M_\parallel = \text{const}, \\ M_x &= M_\perp \cos(-\omega t), \\ M_y &= M_\perp \sin(-\omega t). \end{aligned} \tag{18.14}$$

You can verify that these are a solution for arbitrary values of $M_\perp$ and $M_\parallel$ as long as $\omega = \omega_0 = \gamma B_z$. This is called the *Larmor precession frequency*. The minus sign means that for positive γ the rotation is clockwise in the xy plane. The classical Larmor frequency is equal to the frequency of photons corresponding to the energy difference given by successive values of $\boldsymbol{\mu} \cdot \mathbf{B}$. For this solution the initial values of **M** at $t = 0$ are $M_x(0) = M_\perp$, $M_y(0) = 0$, and $M_z(0) = M_\parallel$.

We need to modify the equation of motion, Eq. 18.12, to include changes in **M** that occur because of effects other than the magnetic field. Suppose that **M** has somehow been changed so that it no longer points along the z axis with the equilibrium value given by Eq. 18.10. Thermal agitation will change the populations of the levels so that M_z returns to the equilibrium value, which we call M_0. We *postulate* that the rate of exchange of energy with the reservoir is proportional to how far the value of M_z is from equilibrium:

$$\frac{dM_z}{dt} = \frac{1}{T_1}\,(M_0 - M_z)\,.$$

The quantity T_1, which is the inverse of the proportionality constant, is called the *longitudinal relaxation time* or *spin–lattice relaxation time*.

We also *postulate* an exponential disappearance of the x and y components of **M** with a *transverse relaxation time* T_2 (sometimes called the *spin–spin relaxation time*). (This assumption is often not a good one. For example, the decay of M_x and M_y in ice is more nearly Gaussian than exponential.) The equations are

$$\frac{dM_x}{dt} = -\frac{M_x}{T_2}, \qquad \frac{dM_y}{dt} = -\frac{M_y}{T_2}.$$

The transverse relaxation time is always shorter than T_1. Here is why. A change of M_z requires an exchange of energy with the reservoir. This is not necessary for changes confined to the xy plane, since the potential energy $(\boldsymbol{\mu} \cdot \mathbf{B})$ does not change in that case. M_x and M_y can change as M_z

changes, but they can also change by other mechanisms, such as when individual spins precess at slightly different frequencies, a process known as *dephasing*. The angular velocity of precession can be slightly different for different nuclear spins because of local variations in the static magnetic field; the angular velocity can also fluctuate as the field fluctuates with time. These variations and fluctuations are caused by neighboring atomic or nuclear magnetic moments or by inhomogeneities in the external magnetic field. Figure 18.4 shows how dephasing occurs if several magnetic moments precess at different rates.

Combining these approximate equations for relaxation in the absence of an applied magnetic field with Eq. 18.12 for the effect of a magnetic field gives the *Bloch equations*:[2]

$$\begin{aligned} \frac{dM_z}{dt} &= \frac{1}{T_1}(M_0 - M_z) + \gamma\,(\mathbf{M}\times\mathbf{B})_z\,, \\ \frac{dM_x}{dt} &= -\frac{M_x}{T_2} + \gamma\,(\mathbf{M}\times\mathbf{B})_x\,, \\ \frac{dM_y}{dt} &= -\frac{M_y}{T_2} + \gamma\,(\mathbf{M}\times\mathbf{B})_y\,. \end{aligned} \tag{18.15}$$

While these equations are not rigorous and there is no reason for the relaxation to be strictly exponential, they have proven to be quite useful in explaining many facets of nuclear spin magnetic resonance.

One can demonstrate by direct substitution the following solution to Eqs. 18.15 for a static magnetic field **B** along the z axis:

$$\begin{aligned} M_x &= M_0 e^{-t/T_2}\cos(-\omega_0 t), \\ M_y &= M_0 e^{-t/T_2}\sin(-\omega_0 t), \\ M_z &= M_0(1 - e^{-t/T_1}), \end{aligned} \tag{18.16}$$

where $\omega_0 = \gamma B$. This solution corresponds to what happens if **M** is somehow made to precess in the xy plane. (We will see how to accomplish this in Sect. 18.5.) The magnetization in the xy plane is initially M_0, and the amplitude decays exponentially with time constant T_2. The initial value of M_z is zero, and it decays back to M_0 with time constant T_1. A perspective plot of the trajectory of the tip of vector **M** is shown in Fig. 18.5.

[2] Felix Bloch and Edward Purcell shared the 1952 Nobel Prize in physics for their discovery of nuclear magnetic resonance.

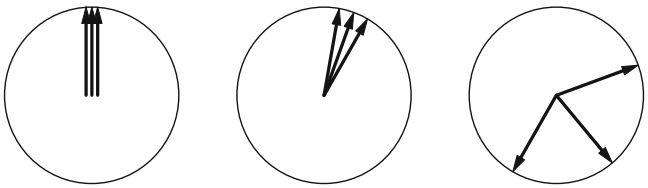

Fig. 18.4 If several spins precess in the xy plane at slightly different rates, the total spin amplitude decreases due to dephasing

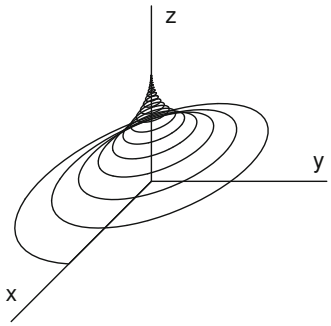

Fig. 18.5 The locus of the tip of the magnetization **M** when it relaxes according to Eqs. 18.16

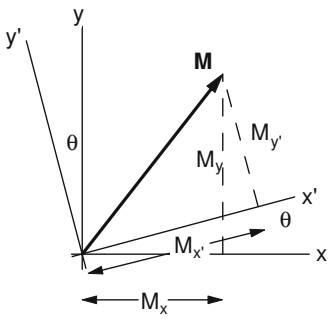

Fig. 18.6 The vector **M** can be represented by components along x and y or along x' and y'

18.5 A Rotating Coordinate System

18.5.1 Transforming to the Rotating Coordinate System

It is *much* easier to describe the motion of **M** in a coordinate system that is rotating about the z axis at the Larmor frequency. Figure 18.6 shows a vector **M** and two coordinate systems, xy and $x'y'$. The z component of **M** is unchanged. By considering the other components in Fig. 18.6, we see that

$$\begin{aligned} M_x &= M_{x'}\cos\theta - M_{y'}\sin\theta, \\ M_y &= M_{x'}\sin\theta + M_{y'}\cos\theta, \\ M_z &= M_{z'}. \end{aligned} \tag{18.17a}$$

This can also be written in matrix form. A rotation through angle θ around the z axis gives $\mathbf{M} = \mathbf{R}\mathbf{M}'$ or

$$\begin{pmatrix} M_x \\ M_y \\ M_z \end{pmatrix} = \begin{pmatrix} \cos\theta & -\sin\theta & 0 \\ \sin\theta & \cos\theta & 0 \\ 0 & 0 & 1 \end{pmatrix} \begin{pmatrix} M_{x'} \\ M_{y'} \\ M_{z'} \end{pmatrix}. \tag{18.17b}$$

Rotations about the other axes are discussed in Problem 12. Note that rotating the coordinate system that describes a fixed vector is equivalent to rotating the vector in the opposite direction, so the results quoted in Problem 12 apply to both situations.

For a three-dimensional coordinate system rotating clockwise around the z axis, $\theta = -\omega t$, the z-component of $\mathbf{M}$ is unchanged, and the transformation equations are

$$\begin{aligned} M_x &= M_{x'}\cos(-\omega t) - M_{y'}\sin(-\omega t), \\ M_y &= M_{x'}\sin(-\omega t) + M_{y'}\cos(-\omega t), \\ M_z &= M_{z'}. \end{aligned} \tag{18.18}$$

The time derivative of $\mathbf{M}$ is obtained by differentiating each component and remembering that $\mathbf{M}'$ can also depend on t:

$$\begin{aligned} \frac{dM_x}{dt} &= \frac{dM_{x'}}{dt}\cos(-\omega t) - \frac{dM_{y'}}{dt}\sin(-\omega t) \\ &\quad + \omega M_{x'}\sin(-\omega t) + \omega M_{y'}\cos(-\omega t), \\ \frac{dM_y}{dt} &= \frac{dM_{x'}}{dt}\sin(-\omega t) + \frac{dM_{y'}}{dt}\cos(-\omega t) \\ &\quad - \omega M_{x'}\cos(-\omega t) + \omega M_{y'}\sin(-\omega t), \\ \frac{dM_z}{dt} &= \frac{dM_{z'}}{dt}. \end{aligned} \tag{18.19}$$

We can use these expressions to write the equations of motion in the rotating frame. First consider a system without relaxation effects and with a static field B_z along the z axis. We will show that the components of $\mathbf{M}$ in a system rotating at the Larmor frequency are constant. The equations of motion are given in Eqs. 18.13. In terms of variables in the rotating frame, the equation for dM_x/dt becomes

$$\begin{aligned} &\frac{dM_{x'}}{dt}\cos(-\omega t) - \frac{dM_{y'}}{dt}\sin(-\omega t) + \omega M_{x'}\sin(-\omega t) \\ &\qquad + \omega M_{y'}\cos(-\omega t) \\ &\quad = \gamma\left[M_{x'}\sin(-\omega t) + M_{y'}\cos(-\omega t)\right]B_z. \end{aligned}$$

If the frame rotates at the Larmor frequency $\omega_0 = \gamma B_z$, the third and fourth terms on the left are equal to the right-hand side. The equation becomes

$$\frac{dM_{x'}}{dt}\cos(-\omega_0 t) - \frac{dM_{y'}}{dt}\sin(-\omega_0 t) = 0.$$

Under the same circumstances, the equation for dM_y/dt gives

$$\frac{dM_{x'}}{dt}\sin(-\omega_0 t) + \frac{dM_{y'}}{dt}\cos(-\omega_0 t) = 0.$$

Solving these simultaneously shows that $dM_{x'}/dt = 0$ and $dM_{y'}/dt = 0$. Therefore, in the rotating system $M_{x'}$ and $M_{y'}$ are constant. Equation 18.13 showed that $M_{z'}$ is constant, so the components of $\mathbf{M}$ are constant in the frame rotating at the Larmor frequency. Using Eqs. 18.18 to transform back to the laboratory system gives the solution Eq. 18.14.[3]

18.5.2 An Additional Oscillating Field

The next problem we consider in the rotating coordinate system is the addition of an oscillating magnetic field $B_1\cos(\omega t)$ along the x axis, fixed in the laboratory system. We will show that if the applied field is at the Larmor frequency, the equations of motion in the rotating system, Eqs. 18.25, are quite simple but very important. They are given below.

They are derived as follows. From the x component of Eq. 18.12, and remembering that $B_y = 0$,

$$\frac{dM_x}{dt} = \gamma M_y B_z,$$

we obtain (remembering that the $x'y'$ system is rotating at the Larmor frequency ω_0)

$$\begin{aligned} &\frac{dM_{x'}}{dt}\cos(-\omega_0 t) - \frac{dM_{y'}}{dt}\sin(-\omega_0 t) \\ &\quad + \omega_0 M_{x'}\sin(-\omega_0 t) + \omega_0 M_{y'}\cos(-\omega_0 t) \\ &= \gamma B_z\left[M_{x'}\sin(-\omega_0 t) + M_{y'}\cos(-\omega_0 t)\right]. \end{aligned}$$

Since $\omega_0 = \gamma B_z$, the last two terms on the left cancel the terms on the right, leaving

$$\frac{dM_{x'}}{dt}\cos(-\omega_0 t) - \frac{dM_{y'}}{dt}\sin(-\omega_0 t) = 0. \tag{18.20}$$

[3] For those familiar with vector analysis, the general relationship between the time derivative of any vector $\mathbf{M}$ in the laboratory system and a system rotating with angular velocity $\boldsymbol{\Omega}$ is

$$\left(\frac{d\mathbf{M}}{dt}\right)_{\text{lab}} = \left(\frac{\partial\mathbf{M}}{\partial t}\right)_{\text{rot}} + \boldsymbol{\Omega}\times\mathbf{M}.$$

This can be applied to the magnetization combined with Eq. 18.12 to give

$$\left(\frac{\partial\mathbf{M}}{\partial t}\right)_{\text{rot}} = \gamma(\mathbf{M}\times\mathbf{B}) - \boldsymbol{\Omega}\times\mathbf{M} = \gamma\mathbf{M}\times\left(\mathbf{B} + \frac{\boldsymbol{\Omega}}{\gamma}\right),$$

which vanishes if $\gamma\mathbf{B} = -\boldsymbol{\Omega}$.

Similarly, the y-component of Eq. 18.12,

$$\frac{dM_y}{dt} = \gamma(M_z B_x - M_x B_z),$$

transforms and reduces to (remembering that $M_z = M_{z'}$)

$$\frac{dM_{x'}}{dt}\sin(-\omega_0 t) + \frac{dM_{y'}}{dt}\cos(-\omega_0 t) = \gamma B_1 M_{z'}\cos(-\omega t). \tag{18.21}$$

The z-component of Eq. 18.12 is, with $B_y = 0$

$$\frac{dM_z}{dt} = -\gamma M_y B_x,$$

which transforms to

$$\frac{dM_{z'}}{dt} = -\gamma B_1 M_{x'}\cos(\omega t)\sin(-\omega_0 t) - \gamma B_1 M_{y'}\cos(\omega t)\cos(-\omega_0 t). \tag{18.22}$$

It is possible to eliminate $M_{x'}$ from Eqs. 18.20 and 18.21 by multiplying Eq. 18.20 by $-\sin(-\omega_0 t)$, multiplying Eq. 18.21 by $\cos(-\omega_0 t)$, and adding. The result is

$$\frac{dM_{y'}}{dt} = \gamma B_1 M_{z'}\cos(\omega t)\cos(-\omega_0 t). \tag{18.23}$$

A similar technique can be used to eliminate $M_{y'}$ from these two equations:

$$\frac{dM_{x'}}{dt} = \gamma B_1 M_{z'}\cos(\omega t)\sin(-\omega_0 t). \tag{18.24}$$

18.5.3 Nutation

Equations 18.22–18.24 are the equations of motion for the components of **M** in the rotating system. If $\omega \neq \omega_0$, the motion is complicated, but averaged over many Larmor periods the right-hand side of each equation is zero. If the applied field oscillates at the Larmor frequency, $\omega = \omega_0$, then the $\cos^2(-\omega_0 t)$ factors average to $\frac{1}{2}$ while factors like $\sin(-\omega_0 t)\cos(-\omega_0 t)$ average to zero.

The averaged equations are a very important result:

$$\frac{dM_{x'}}{dt} = 0, \tag{18.25a}$$

$$\frac{dM_{y'}}{dt} = \frac{\gamma B_1}{2} M_{z'}, \tag{18.25b}$$

$$\frac{dM_{z'}}{dt} = -\frac{\gamma B_1}{2} M_{y'}. \tag{18.25c}$$

The first equation says that if $M_{x'}$ is initially zero, it remains zero. Let us define a new angular frequency

$$\omega_1 = \frac{\gamma B_1}{2}. \tag{18.26}$$

It is the frequency of rotation caused by B_1 oscillating at the Larmor frequency. It is much lower than the Larmor frequency because $B_1 \ll B_z$. In terms of ω_1, Eqs. 18.25b and 18.25c become

$$\frac{dM_{z'}}{dt} = -\omega_1 M_{y'}, \qquad \frac{dM_{y'}}{dt} = \omega_1 M_{z'}.$$

These are a pair of coupled linear differential equations with constant coefficients. Differentiating one and substituting it in the other gives

$$\frac{d^2 M_{z'}}{dt^2} = -\omega_1 \frac{dM_{y'}}{dt} = -\omega_1^2 M_{z'}, \tag{18.27}$$

which has a solution (a and b are constants of integration)

$$M_{z'} = a\sin(\omega_1 t) + b\cos(\omega_1 t). \tag{18.28}$$

From Eq. 18.25c we get

$$M_{y'} = -\frac{1}{\omega_1}\frac{dM_{z'}}{dt} = -a\cos(\omega_1 t) + b\sin(\omega_1 t). \tag{18.29}$$

The values of a and b are determined from the initial conditions. For example, if **M** is initially along the z axis, $a = 0$ and $b = M_0$. Then

$$\begin{aligned} M_{x'} &= 0, \\ M_{y'} &= M_0\sin(\omega_1 t), \\ M_{z'} &= M_0\cos(\omega_1 t). \end{aligned} \tag{18.30}$$

This kind of motion—precession about the z axis combined with a change of the projection of **M** on z—is called *nutation*.

18.5.4 π and π/2 Pulses

From Eqs. 18.30 it is easy to see that turning B_1 on for a quarter of a period of ω_1 (a 90° pulse or $\pi/2$ *pulse*, $t = T/4 = \pi/2\omega_1$) nutates **M** into the $x'y'$ plane, while a 180° or π *pulse* nutates **M** to point along the $-z$ axis. **M** nutates about the rotating x' axis. Shifting the phase of B_1 changes the axis in the $x'y'$ plane about which **M** nutates. It may seem strange that an oscillating magnetic field pointing along an axis fixed in the laboratory frame causes rotation about an axis in the rotating frame. The reason is that B_1 is also oscillating at the Larmor frequency, so that its amplitude changes in just the right way to cause this behavior of **M**. Figures 18.7 and 18.8 show this nutation in both the rotating frame and the laboratory frame for a $\pi/2$ pulse and a π pulse.

Figure 18.7c emphasizes the difference between nutation and relaxation by plotting M_z vs. the projection of **M** in the $x'y'$ plane. For nutation the components of **M** are given by

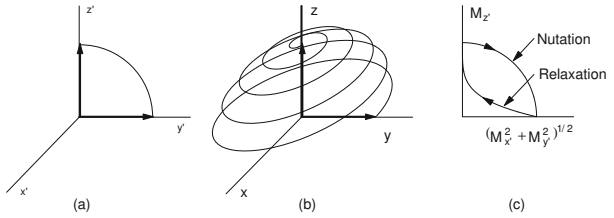

Fig. 18.7 The locus of the tip of the magnetization **M** when an oscillating magnetic field B_1 is applied for a time t such that $\omega_1 t = \pi/2$. This is often called a "$\pi/2$" pulse. **a** The rotating frame. **b** The laboratory frame. **c** Plots of $M_{z'}$ vs $(M_{x'}^2 + M_{y'}^2)^{1/2}$ showing the difference between nutation and relaxation

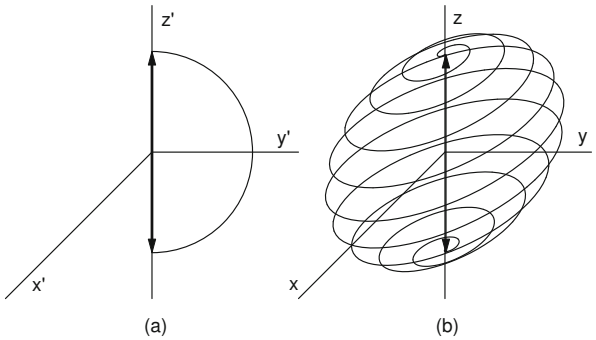

Fig. 18.8 A "π pulse" B_1 is applied for a time $t = \pi/\omega_1$ and rotates **M** to point along the $-z$ axis. **a** The rotating frame. **b** The laboratory frame

Eqs. 18.30, the magnitude of **M** is unchanged, and the locus is a circle. For relaxation the components are given by Eqs. 18.16.

Another interesting solution is one for which the initial value of **M** is

$$M_{x'}(0) = M_0 \cos\alpha,$$

$$M_{y'}(0) = M_0 \sin\alpha,$$

$$M_{z'}(0) = 0.$$

This corresponds to an **M** that has already been nutated into the $x'y'$ plane. Substituting these values in Eqs. 18.28 and 18.29 shows that $b = 0$ and $a = M_0 \sin\alpha$. Then the solution is

$$M_{x'}(t) = M_0 \cos\alpha,$$

$$M_{y'}(t) = M_0 \sin\alpha \cos(\omega_1 t), \tag{18.31}$$

$$M_{z'}(t) = -M_0 \sin\alpha \sin(\omega_1 t).$$

This solution is plotted in Fig. 18.9 in both the rotating frame and the laboratory frame for the case of a π pulse (a pulse of duration π/ω_1). The effect is to nutate **M** about the x' axis in the rotating coordinate system. We will see later that this is a very useful pulse.

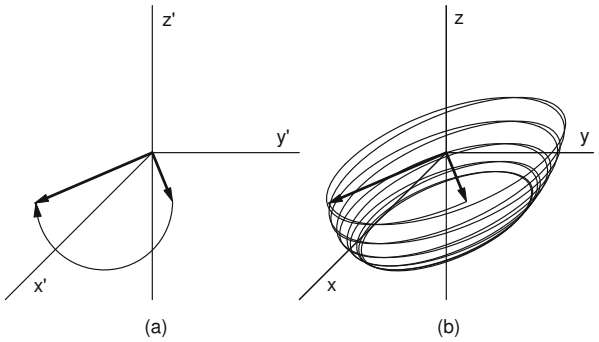

Fig. 18.9 A magnetic field B_1 pointing along the laboratory x axis and oscillating at the Larmor frequency causes nutation of **M** through an angle π around the rotating x' axis. In this case **M** was initially in the $x'y'$ plane. The motion shown here is plotted from Eqs. 18.30 in the rotating (**a**) and the laboratory (**b**) frames

18.6 Relaxation Times

Since longitudinal relaxation changes the value of M_z and hence $\boldsymbol{\mu} \cdot \mathbf{B}$, it is associated with a change of energy of the nucleus. The principal force that can do work on the nuclear spin and change its energy arises from the fact that the nucleus is in a fluctuating magnetic field due to neighboring nuclei and the electrons in paramagnetic atoms.

One way to analyze the effect of this magnetic field is to say that the change of spin energy E is accompanied by the emission or absorption of a photon of frequency $\nu_{\text{photon}} = E/h$, or $\omega_{\text{photon}} = \omega_0$. An increase of spin energy requires the absorption of a photon at the Larmor frequency (*stimulated absorption*). This will have a high probability if the fluctuating magnetic field has a large Fourier component at the Larmor frequency. A decrease of spin energy is accompanied by the emission of a photon. This can happen spontaneously in a vacuum (*spontaneous emission*), or it can be stimulated by the presence of other photons at the Larmor frequency (*stimulated emission*). These relative probabilities can be calculated using quantum mechanics. Stimulated emission or absorption is much more probable than is spontaneous emission.

The random magnetic field at a nucleus fluctuates because of the movement of the nucleus in the magnetic field of nearby atoms and nuclei. If the field changes rapidly enough, it will have Fourier components at the Larmor frequency that can induce transitions that cause M_z to change by absorption or emission. To get an idea of the strength of the field involved, consider the field at one hydrogen nucleus in a water molecule due to the other hydrogen nucleus. The field due to a magnetic dipole is given by

$$B_r = \frac{\mu_0}{4\pi} \frac{2\mu}{r^3} \cos\theta,$$

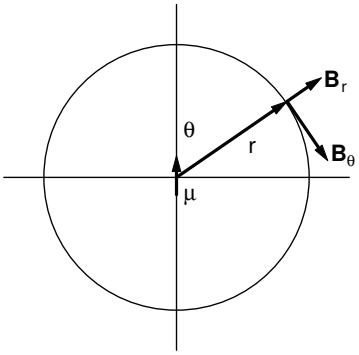

Fig. 18.10 The magnetic field components of a dipole in spherical coordinates point in the directions shown

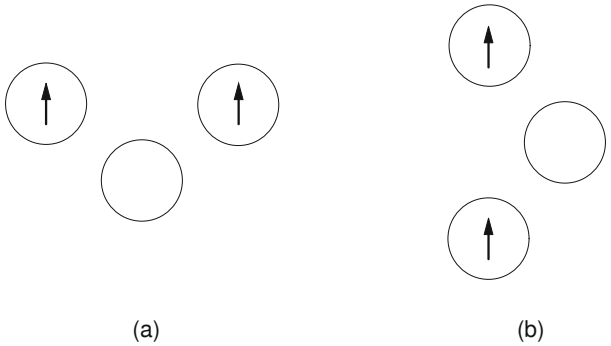

Fig. 18.11 The z components of the magnetic moments of two protons in a water molecule are shown for two different molecular orientations, **a** and **b**. When the water molecule is fixed in space, as in ice, the magnetic field that one proton produces in the neighborhood of the other is static. When the water molecule tumbles, as in a liquid or gas, the field that one proton produces at the other changes with time

$$B_\theta = \frac{\mu_0}{4\pi}\frac{\mu}{r^3}\sin\theta, \qquad (18.32)$$
$$B_\phi = 0,$$

where angle θ is defined in Fig. 18.10. (The factor $\mu_0/4\pi \equiv 10^{-7}$ T m A^{-1} is required in SI units.) The magnetic field at one hydrogen nucleus in a water molecule due to the other hydrogen nucleus is about 4×10^{-4} T (see Problem 14). Consider the water molecule shown in Fig. 18.11. We refer to each hydrogen nucleus as a proton. The z components of the proton magnetic moments are shown. If the water molecule is oriented as in Fig. 18.11a, the field at one proton due to the other has a certain value. If the water molecule remains fixed in space, as in ice, the field is constant with time. If the molecule is tumbling, as in liquid water, the orientation changes as in Fig. 18.11b, and the field changes with time.

When the molecules are moving randomly, the fluctuating magnetic field components are best described by their autocorrelation functions. The simplest assumption one can make[4] is that the autocorrelation function ϕ_{11} of each magnetic field component is exponential and that each field component has the same correlation time τ_C:

$$\phi_{11}(\tau) \propto e^{-|\tau|/\tau_C}. \qquad (18.33)$$

The Fourier transform of the autocorrelation function gives the power at different frequencies. It has only cosine terms because the autocorrelation is even. Comparison with the Fourier transform pair of Eq. 11.101 shows that the power at frequency ω is proportional to $\tau_C/(1+\omega^2\tau_C^2)$. With the assumption that the transition rate, which is $1/T_1$, is proportional to the power at the Larmor frequency, we have (see also Slichter 1990 or Levitt 2008)

$$\frac{1}{T_1} = \frac{C\tau_C}{1+\omega_0^2\tau_C^2}, \qquad (18.34)$$

where C is the proportionality constant.

The correlation time in a solid is much longer than in a liquid. For example, in liquid water at 20 °C it is about 3.5×10^{-12} s; in ice it is about 2×10^{-6} s. Figure 18.12 shows the behavior of T_1 as a function of correlation time, plotted from Eq. 18.34 with $C = 5.43\times10^{10}$ s^{-2}. For short correlation times T_1 does not depend on the Larmor frequency. At long correlation times T_1 is proportional to the square of the Larmor frequency, as can be seen from Eq. 18.34. The minimum in T_1 occurs when $\omega_0 = 1/\tau_C$ in this model.

Table 18.2 shows some typical values of the relaxation times for a Larmor frequency of 20 MHz. Neighboring paramagnetic atoms reduce the relaxation time by causing a fluctuating magnetic field. For example, adding 20 ppm of Fe^{3+} to pure water reduces T_1 from 3000 to 20 ms.

Differences in relaxation time are easily detected in an image. Different tissues have different relaxation times. A contrast agent containing gadolinium (Gd^{3+}), which is strongly paramagnetic, is often used in magnetic resonance imaging. It is combined with many of the same pharmaceuticals used with ^{99m}Tc, and it reduces the relaxation time of nearby nuclei. Gadolinium has been used to assess ischemic myocardium (Sakuma 2007). Iron oxide nanoparticles are sometimes used to create contrast in magnetic resonance images (Kim et al. 2011).

The hemoglobin that carries oxygen in the blood exists in two forms: oxyhemoglobin and deoxyhemoglobin. The former is diamagnetic and the latter is paramagnetic, so the relaxation time in blood depends on the amount of oxygen in the hemoglobin. The imaging technique that exploits this is called BOLD (blood oxygen level dependent).

[4] A more complete model recognizes that different atoms experience fluctuating fields with different correlation times and that frequency components at twice the Larmor frequency also contribute.

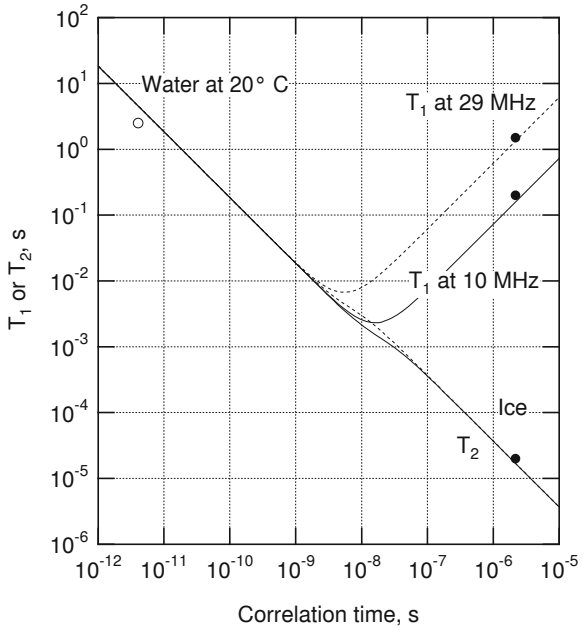

Fig. 18.12 Plot of T_1 and T_2 vs correlation time of the fluctuating magnetic field at the nucleus. The dashed lines are for a Larmor frequency of 29 MHz; the solid lines are for 10 MHz. Experimental points are shown for water (open dot) and ice (solid dots)

Table 18.2 Approximate relaxation times at 20 MHz

	T_1 (ms)	T_2 (ms)
Whole blood	900	200
Muscle	500	35
Fat	200	60
Water	3000	3000

The same model for the fluctuating fields which led to Eq. 18.34 gives an expression for T_2:

$$\frac{1}{T_2} = \frac{C\tau_C}{2} + \frac{1}{2T_1}, \qquad (18.35)$$

$$T_2 = \frac{2}{C\tau_C}\left[\frac{1+\omega_0^2\tau_C^2}{2+\omega_0^2\tau_C^2}\right].$$

There is a slight frequency dependency to T_2 for values of the correlation time close to the reciprocal of the Larmor frequency.

Another effect that causes the magnetization to rapidly decrease is *dephasing*. Dephasing across the sample occurs because of inhomogeneities in the externally applied field. Suppose that the spread in Larmor frequency and the transverse relaxation time are related by $T_2\Delta\omega = K$. (Usually K is taken to be 2.) The spread in Larmor frequencies $\Delta\omega$ is due to a spread in magnetic field ΔB experienced by the nuclear spins in different atoms. The total variation in B is due to fluctuations caused by the magnetic field of neighbors and to variation in the applied magnetic field across the sample:

$$\Delta B_{\text{tot}} = \Delta B_{\text{internal}} + \Delta B_{\text{external}}.$$

Therefore

$$\Delta\omega_{\text{tot}} = \Delta\omega_{\text{internal}} + \Delta\omega_{\text{external}}.$$

The total spread is associated with the experimental relaxation time, $T_2^* = K/\Delta\omega_{\text{tot}}$. The *true* or *nonrecoverable* relaxation time $T_2 = K/\Delta\omega_{\text{internal}}$ is due to the fluctuations in the magnetic field intrinsic to the sample. Therefore

$$\frac{1}{T_2^*} = \frac{1}{T_2} + \frac{\gamma\Delta B_{\text{external}}}{K}. \qquad (18.36)$$

T_2 is called the nonrecoverable relaxation time because various experimental techniques can be used to compensate for the external inhomogeneities, but not the internal atomic ones.

18.7 Detecting the Magnetic Resonance Signal

We have now seen that a sample of nuclear spins in a strong magnetic field has an induced magnetic moment; that it is possible to apply a sinusoidally varying magnetic field and nutate the magnetic moment to precess at any arbitrary angle with respect to the static field; and that the magnetization then relaxes or returns to its original state with two characteristic time constants, the longitudinal and transverse relaxation times. We next consider how a useful signal can be obtained from these spins. This is done by measuring the weak magnetic field generated by the magnetization as it precesses in the xy plane.

Suppose that a sample is at the origin. The motions plotted in Fig. 18.7 suggest that one way to produce a magnetization rotating in the xy plane is to have a static field along the z axis, combined with a coil in the yz plane (perpendicular to the x axis) connected to a generator of alternating current at frequency ω_0. Turning on the generator for a time $\Delta t = \pi/2\omega_1 = \pi/\gamma B_1$ rotates the magnetization into the xy plane (a 90° or $\pi/2$ pulse). If the generator is then turned off, the same coil can be used to detect the changing magnetic flux due to the rotating magnetic moments. The resulting signal, an exponentially damped sine wave, is called the *free induction decay* (FID).

To estimate the size of the signal induced in the coil, imagine a magnetic moment $\boldsymbol{\mu} = \mathbf{M}\Delta V$ rotating in the xy plane as shown in Fig. 18.13. The voltage v induced in a one-turn coil in the yz plane is the rate of change of the magnetic flux through the coil:

$$v = -\frac{\partial\Phi}{\partial t} = -\frac{\partial}{\partial t}\iint \mathbf{B}\cdot d\mathbf{S}.$$

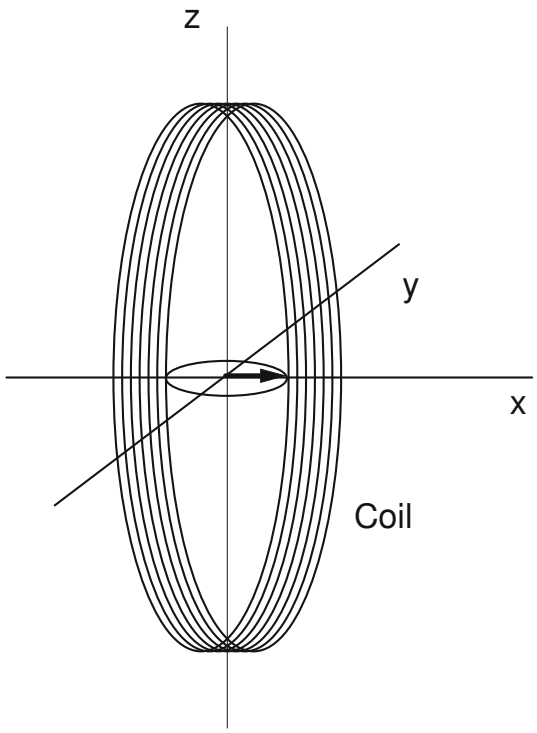

Fig. 18.13 A magnetic moment rotating in the xy plane induces a voltage in a pickup coil in the yz plane. The coil is viewed from slightly to the right of the coil

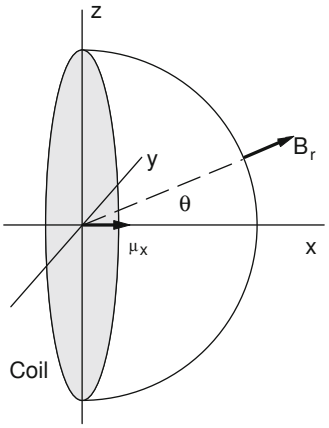

Fig. 18.14 A dipole along the x axis generates a flux through the shaded circle in the yz plane that is equal and opposite to that through the hemispherical cap. The drawing is viewed from slightly to the right of the yz plane

The magnetic field far from a magnetic dipole can be written most simply in spherical coordinates (Eqs. 18.32). We need the flux through the coil of radius a in the yz plane. However, Eqs. 18.32 are not valid close to the dipole. Since a fundamental property of the magnetic field is that for a closed surface $\iint \mathbf{B}\cdot d\mathbf{S} = 0$, the flux through the coil in Fig. 18.13 is the negative of the flux Φ through the hemispherical cap in Fig. 18.14:

$$\Phi = -\int B_r 2\pi a^2 \sin\theta\, d\theta = -\frac{\mu_0}{4\pi}\frac{4\pi\mu_x}{a}\int_0^{\pi/2} \cos\theta\, \sin\theta\, d\theta$$
$$= -\frac{\mu_0}{4\pi}\frac{2\pi\mu_x}{a}. \qquad (18.37)$$

At any instant $\boldsymbol{\mu}$ can be resolved into components along x and y. The component pointing along y contributes no net flux through the spherical cap of Fig. 18.14. Therefore, the flux for a magnetic moment $\boldsymbol{\mu} = \mathbf{M}\Delta V$, where $\mathbf{M}$ is given by Eqs. 18.16, is

$$\Phi = -\frac{\mu_0}{4\pi}\frac{2\pi M_0 \Delta V}{a} e^{-t/T_2}\cos(-\omega_0 t).$$

The induced voltage is $-\partial\Phi/\partial t$:

$$v = \frac{\mu_0}{4\pi}\frac{2\pi M_0 \Delta V}{a} e^{-t/T_2}\left(-\frac{1}{T_2}\cos(-\omega_0 t) + \omega_0 \sin(-\omega_0 t)\right).$$

Since $1/T_2 \ll \omega_0$, this can be simplified to

$$v = -\frac{\mu_0}{4\pi}\frac{\omega_0}{a} 2\pi M_0 \Delta V\, e^{-t/T_2}\sin(-\omega_0 t).$$

If the value of M_z which exists at thermal equilibrium has been nutated into the xy plane, then M_0 is given by the M_z of Eq. 18.10. For a spin-$\frac{1}{2}$ particle (and using the fact that $\omega_0 = \gamma B_0$) we obtain

$$v = -\frac{\mu_0}{4\pi}\frac{\pi N\, \Delta V\, \gamma^3 \hbar^2 B_0^2}{2k_B T a} e^{-t/T_2}\sin(-\omega_0 t). \qquad (18.38)$$

Here $N\,\Delta V$ is the total number of nuclear spins involved, B_0 is the field along the z axis, and a is the radius of the coil that detects the free-induction-decay signal. For a volume element of fixed size, as in magnetic resonance imaging, the sensitivity is inversely proportional to the coil radius. If the sample fills the coil, as in most laboratory spectrometers, then $\Delta V \propto a^2$ and the sensitivity is proportional to a. Because the signal in Eq. 18.38 is proportional to the square of the magnetic field B_0, there has been a push for higher and higher magnetic field strengths; 7 T is typical for high B_0 studies (Robitaille and Berliner 2006).

18.8 Some Useful Pulse Sequences

Many different ways of applying radio-frequency pulses to generate B_1 have been developed by nuclear magnetic resonance spectroscopists for measuring relaxation times. There are five "classic" sequences, which also form the basis for magnetic resonance imaging.

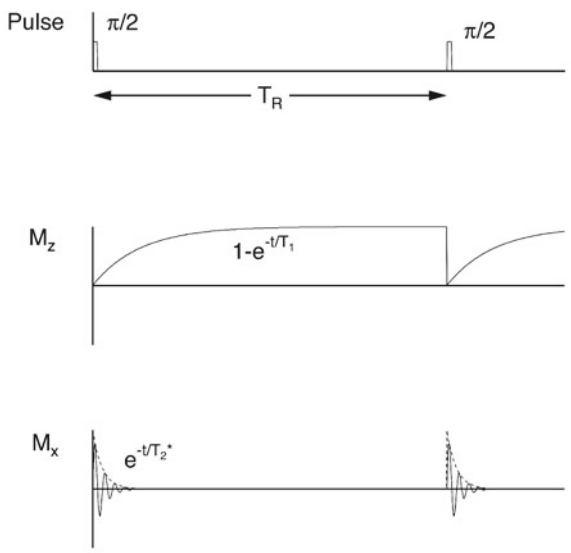

Fig. 18.15 Pulse sequence and signal for a free-induction-decay measurement

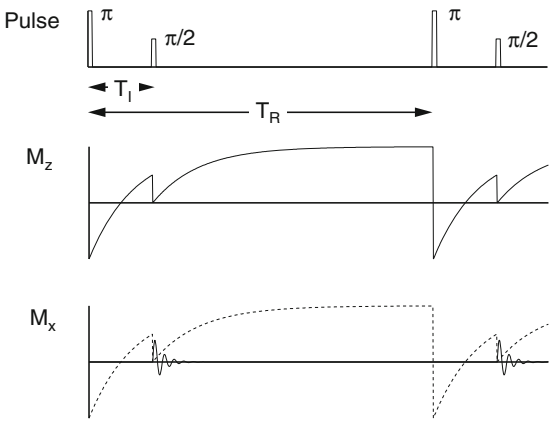

Fig. 18.16 The inversion recovery sequence allows determination of T_1 by making successive measurements at various values of the interrogation time T_I

18.8.1 Free-Induction-Decay (FID) Sequence

Free induction decay was described in Sect. 18.7. A $\pi/2$ pulse nutates **M** into the xy plane, where its precession induces a signal in a pickup coil. The signal is of the form $e^{-(t/T_2^*)}\sin(-\omega_0 t)$, where T_2^* is the experimental transverse relaxation time, including magnetic field inhomogeneities due to the apparatus as well as those intrinsic to the sample. Figure 18.15 shows the pulse sequence, the value of M_x, and the value of M_z. The signal is proportional to M_x. The pulses can be repeated after time T_R for signal averaging. It is necessary for T_R to be greater than, say, $5T_1$ in order for M_z to return nearly to its equilibrium value between pulses.

18.8.2 Inversion-Recovery (IR) Sequence

The inversion-recovery sequence allows measurement of T_1. A π pulse causes **M** to point along the $-z$ axis. There is not yet any signal at this time. M_z returns to equilibrium according to $M_z = M_0\left[1-2e^{-(t/T_1)}\right]$. A $\pi/2$ interrogation pulse at time T_I rotates the instantaneous value of M_z into the xy plane, thereby giving a signal proportional to $M_0\left[1-2e^{-(T_I/T_1)}\right]$, as shown in Fig. 18.16. The process can be repeated; again the repeat time must exceed $5T_1$.

You can see from Fig. 18.16 that there will be no signal at all if $T_I/T_1 = 0.693$. If T_I is less than this, the M_x signal will be inverted (negative). Unless special detector circuits are used which allow one to determine that M_x is negative, the results can be confusing.

Inversion recovery images take a long time to acquire and there is ambiguity in the sign of the signal. There are also problems with the use of a π pulse for slice selection (defined in Sect. 18.9; the details of the problems are found in Joseph et al. 1984).

18.8.3 Spin-Echo (SE) Sequence

The pulse sequence shown in Fig. 18.17 can be used to determine T_2 rather than T_2^*. Initially a $\pi/2$ pulse nutates **M** about the x' axis so that all spins lie along the rotating y' axis. Figure 18.17a shows two such spins. Spin **a** continues to precess at the same frequency as the rotating coordinate system; spin **b** is subject to a slightly smaller magnetic field and precesses at a slightly lower frequency, so that at time $T_E/2$ it has moved clockwise in the rotating frame by angle θ, as shown in Fig. 18.17b. At this time a π pulse is applied that rotates all spins around the x' axis. Spin **a** then points along the $-y'$ axis; spin **b** rotates to the angle shown in Fig. 18.17c. If spin **b** still experiences the smaller magnetic field, it continues to precess clockwise in the rotating frame. At time T_E both spins are in phase again, pointing along $-y'$ as shown in Fig. 18.17d. The resulting signal is called an *echo*, and the process for producing it is called a *spin-echo sequence*. The formation of an echo depends only on the fact that the magnetic field at the nucleus remained the same before and after the π pulse; it does not depend on the specific value of the dephasing angle. Therefore all of the spin dephasing that has been caused by a time-independent magnetic field is reversed in this process. There remains only the dephasing caused by fluctuating magnetic fields. Figure 18.18 shows the pulse sequence and signal.

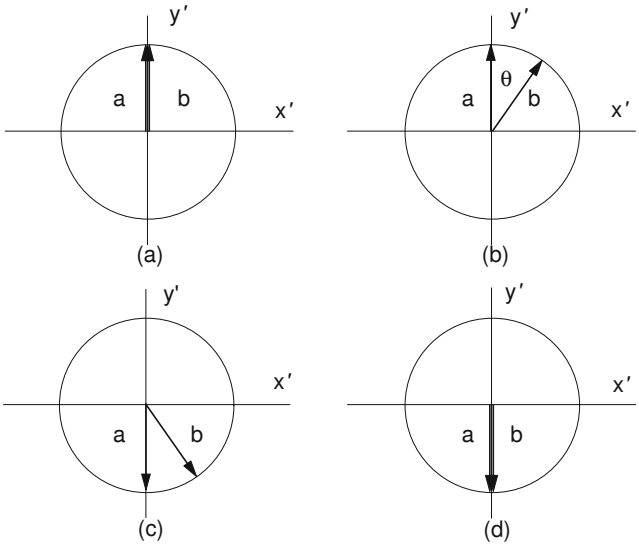

Fig. 18.17 Two magnetic moments are shown in the $x'y'$ plane in the rotating coordinate system. Moment **a** rotates at the Larmor frequency and remains aligned along the y' axis. Moment **b** rotates clockwise with respect to moment **a**. **a** Both moments are initially in phase. **b** After time $T_E/2$ moment **b** is clockwise from moment **a**. **c** A π pulse nutates both moments about the x' axis. **d** At time T_E both moments are in phase again

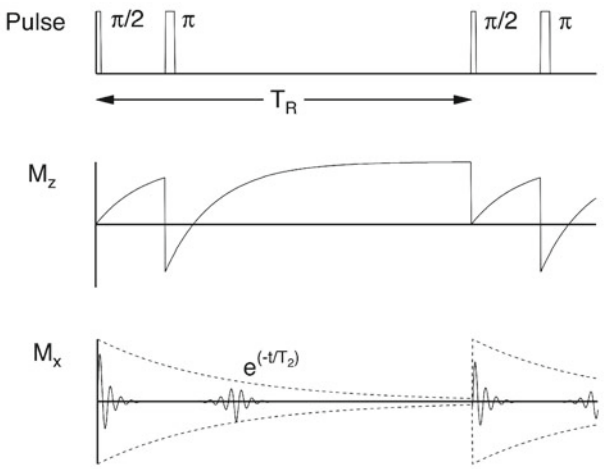

Fig. 18.18 The pulse sequence and magnetization components for a spin-echo sequence

18.8.4 Carr–Purcell (CP) Sequence

When a sequence of π pulses that nutate **M** about the x' axis are applied at $T_E/2$, $3T_E/2$, $5T_E/2$, etc., a sequence of echoes are formed, the amplitudes of which decay with relaxation time T_2. This is shown in Fig. 18.19. Referring to Fig. 18.17, one can see that the echoes are aligned alternately

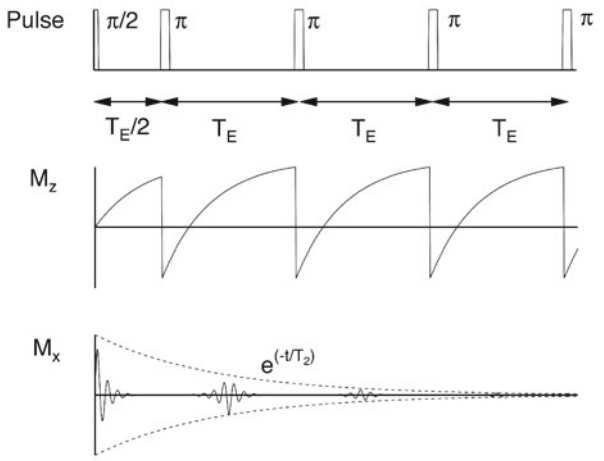

Fig. 18.19 The Carr–Purcell pulse sequence. All pulses nutate about the x' axis. Echoes alternate sign. The envelope of echoes decays as e^{-t/T_2}, where T_2 is the unrecoverable transverse relaxation time

along the $-y'$ and $+y'$ axes. One advantage of the Carr–Purcell sequence is that it allows one to determine rapidly many points on the decay curve. Another advantage relates to diffusion. The molecules that contain the excited nuclei may diffuse. If the external magnetic field B_0 is not uniform, the molecules can diffuse to another region where the magnetic field is slightly different. As a result the rephasing after a pulse does not completely cancel the initial dephasing. This effect is reduced by the Carr–Purcell sequence (see Problem 47).

18.8.5 Carr–Purcell–Meiboom–Gill (CPMG) Sequence

One disadvantage of the CP sequence is that the π pulse must be very accurate or a cumulative error builds up in successive pulses. The Carr–Purcell–Meiboom–Gill sequence overcomes this problem. The initial $\pi/2$ pulse nutates **M** about the x' axis as before, but the subsequent pulses are shifted a quarter cycle in time, which causes them to rotate about the y' axis. This is shown in Fig. 18.20. To see why this pulse sequence (Fig. 18.21) is less sensitive to errors in the duration of the π pulses, consider moment **a**. In the CP sequence, Fig. 18.17, a π pulse that is too long will nutate **a** too far, and it will have a smaller component in the $x'y'$ plane. The next pulse will nutate it even further. In Fig. 18.20, the π pulses will not affect moment **a** at all. This is explored further in Problems 29 and 30.

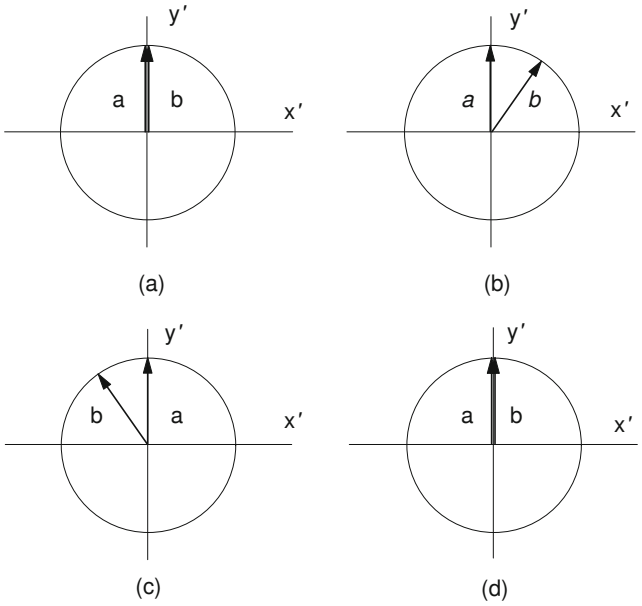

Fig. 18.20 The effect of the Carr–Purcell–Meiboom–Gill pulse sequence on the magnetization. This is similar to Fig. 18.17 except that the π pulses rotate around the y' axis. Moment **b** rotates clockwise in the $x'y'$ plane. **a** Both moments are initially in phase. **b** After time $T_E/2$ moment **b** is clockwise from moment **a**. **c** A π pulse rotates both moments about the y' axis. **d** At time T_E both moments are in phase again

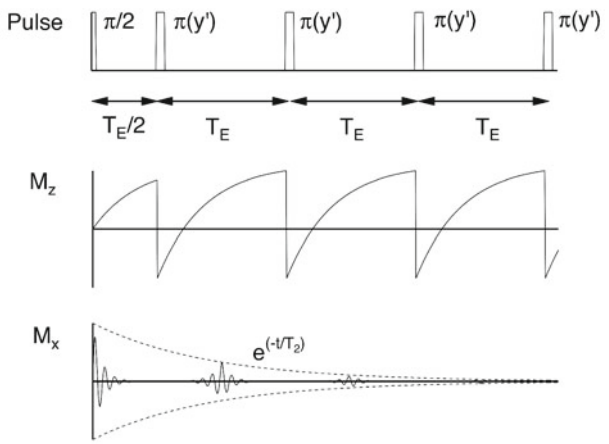

Fig. 18.21 The CPMG pulse sequence

18.9 Imaging

Many more techniques are available for imaging with magnetic resonance than for x-ray computed tomography. They are described by Brown et al. (1994), by Choet al. (1993), by Vlaardingerbroek and den Boer (2004), and by Liang and Lauterbur (2000). One of these authors, Paul C. Lauterbur, shared with Sir Peter Mansfield the 2003 Nobel Prize in physiology or medicine for the invention of magnetic resonance imaging.

Creation of the images requires the application of gradients in the static magnetic field B_z which cause the Larmor frequency to vary with position. The first gradient is applied in the z direction during the $\pi/2$ pulse so that only the spins in a slice in the patient are *selected* (nutated into the xy plane). Slice selection is followed by gradients of B_z in the x and y directions. These also change the Larmor frequency. If the gradient is applied during the readout, the Larmor frequency of the signal varies as B_z varies with position. If the gradient is applied before the readout, it causes a position-dependent phase shift in the signal which can be detected.

We discuss several reconstruction methods here. *Projection reconstruction* is similar to CT reconstruction, but it is slow and rarely used. A two-dimensional Fourier technique known as *spin warp* or *phase encoding* forms the basis of the techniques used in most machines. We also describe briefly some techniques that are even faster. Finally, we discuss how the image contrast can be modified by changing the pulse sequence parameters.

Our initial discussion is based on a spin-echo pulse sequence, repeated with a repetition time T_R as shown in Fig. 18.18.

18.9.1 Slice Selection

First, suppose we simply apply a $\pi/2$ pulse to the entire sample in a 1.5-T machine ($\omega_0 = 401 \times 10^6$ s^{-1}; $\nu_0 = 63.9$ MHz). If the duration of this pulse is to be, say, 5 ms, it requires a constant amplitude of the radio-frequency magnetic field

$$B_1 = \pi/\gamma\,\Delta t = 2.35 \times 10^{-6}\ \mathrm{T}. \tag{18.39}$$

The pulse lasts for 3×10^5 cycles at the Larmor frequency. The frequency spread of the pulse is about 200 Hz. This excites all the proton spins in the entire sample.

For MR imaging, we want to select a thin slice in the sample. In order to select a thin slice (say $\Delta z = 1$ cm) we apply a magnetic field gradient in the z direction while applying a specially shaped B_1 signal. In a static magnetic field B_0, the field lines are parallel. The field strength is proportional to the number of lines per unit area and does not change. With the gradient applied in the volume of interest, the field lines converge, and the field increases linearly with z as shown in Fig. 18.22a, b:

$$B_z(z) = B_0 + G_z z. \tag{18.40}$$

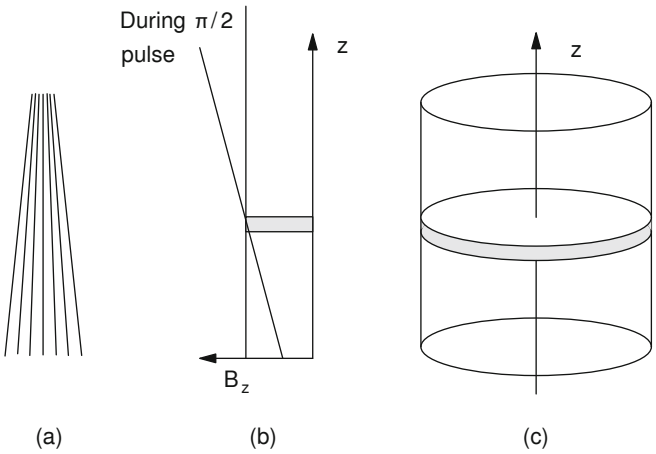

Fig. 18.22 **a** Magnetic field lines for a magnetic field that increases in the z direction. **b** A plot of B_z vs z with and without a gradient. **c** After application of a field gradient in the z direction during the specially shaped rf pulse, all of the spins in the shaded *slice* are excited, that is, they are precessing in the xy plane

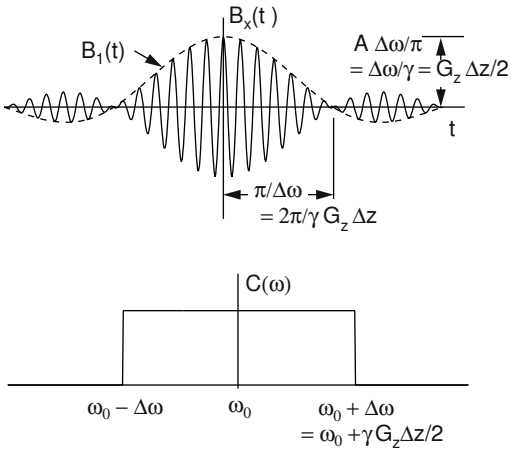

Fig. 18.23 **a** The $B_x(t)$ signal shown is used to selectively excite a slice. It consists of $\cos(\omega_0 t)$ modulated by a $\mathrm{sinc}(x)$ or $\sin(x)/x$ pulse $B_1(t)$. **b** The frequency spectrum contains a uniform distribution of frequencies

We adopt a notation in which **G** represents a partial derivative of the z component of the magnetic field:

$$\mathbf{G} = \begin{pmatrix} G_x \\ G_y \\ G_z \end{pmatrix} = \begin{pmatrix} \partial B_z/\partial x \\ \partial B_z/\partial y \\ \partial B_z/\partial z \end{pmatrix}. \tag{18.41}$$

In a typical machine, $G_z = 5\times10^{-3}$ T m^{-1}. For a slice thickness $\Delta z = 0.01$ m, the Larmor frequency across the slice varies from $\omega_0 - \Delta\omega$ to $\omega_0 + \Delta\omega$, where $\Delta\omega = \gamma G_z \Delta z/2 = 6.68 \times 10^3$ s^{-1} ($\Delta f = 1.064$ kHz).

It is possible to make the signal $B_x(t)$ consist of a uniform distribution of frequencies between $\omega_0 - \Delta\omega$ and $\omega_0 + \Delta\omega$, so that all protons are excited in a slice of thickness Δz from $-\Delta z/2$ to $+\Delta z/2$. Let the amplitude of B_x in the interval $(\omega, d\omega)$ be A. Using Eq. 11.57, $B_x(t)$ is given by

$$\begin{aligned} B_x(t) &= \frac{A}{2\pi}\int_{\omega_0-\Delta\omega}^{\omega_0+\Delta\omega} \cos(\omega t)\, d\omega \\ &= \frac{A\Delta\omega}{\pi}\frac{\sin(\Delta\omega t)}{\Delta\omega t}\cos(\omega_0 t). \end{aligned} \tag{18.42}$$

This has the form $B_1(t)\cos(\omega_0 t)$, where $B_1(t) = (A\Delta\omega/\pi)\sin(\Delta\omega t)/(\Delta\omega t)$. The function $\sin(x)/x$ has its maximum value of 1 at $x = 0$. It is also called the $\mathrm{sinc}(x)$ function. The angle ϕ through which the spins are nutated is

$$\begin{aligned} \phi &= \int_{-\infty}^{\infty} \omega_1(t)\, dt = \frac{\gamma}{2}\int_{-\infty}^{\infty} B_1(t)\, dt \\ &= \frac{\gamma A\Delta\omega}{2\pi}\int_{-\infty}^{\infty}\frac{\sin(\Delta\omega t)}{\Delta\omega t}\, dt \\ &= \frac{\gamma A}{2}. \end{aligned}$$

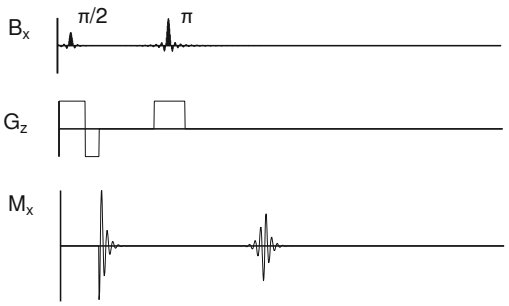

Fig. 18.24 A slice selection pulse sequence. While a gradient G_z is applied, a $\pi/2$ B_x (rf) pulse nutates the spins in a slice of thickness Δz into the xy plane. A negative G_z gradient restores the phase of the precessing spins. The echo after the π pulse is from the entire slice

For a $\pi/2$ pulse, $A = \pi/\gamma$. The maximum value of B_1 is therefore $\Delta\omega/\gamma = G_z\Delta z/2$, as shown in Fig. 18.23. The B_x pulse does not have an abrupt beginning; it grows and decays as shown. In practice, it is truncated at some distance from the peak where the lobes are small.

While the gradient is applied, the transverse components of spins at different values of z precess at different rates (see Problem 35). Therefore it is necessary to apply a gradient G_z of opposite sign after the $\pi/2$ pulse is finished in order to bring the spins back to the phase they had at the peak of the slice selection signal. The gradient is removed when all of the spins in the slice shown in Fig. 18.22c are back in phase. They then continue to precess in the xy plane at the Larmor frequency. This gives the first M_x pulse in Fig. 18.24. The complicated behavior of M_x during the slice selection gradient is not shown. This initial free-induction-decay pulse is not used for imaging.

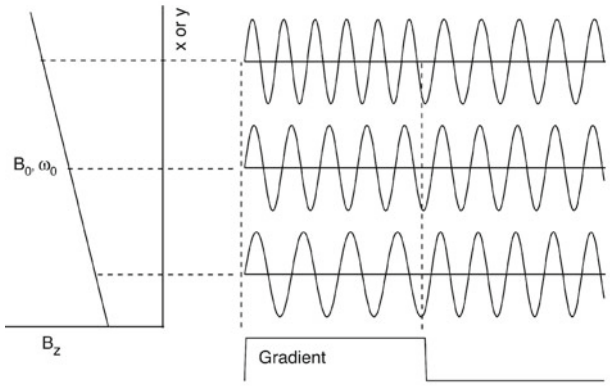

Fig. 18.25 A gradient in B_z causes the Larmor frequency to vary with position. If the signal is measured while the gradient is applied, the Larmor frequency varies with position. If the signal is measured after the gradient has been applied and removed, a position-dependent phase shift remains

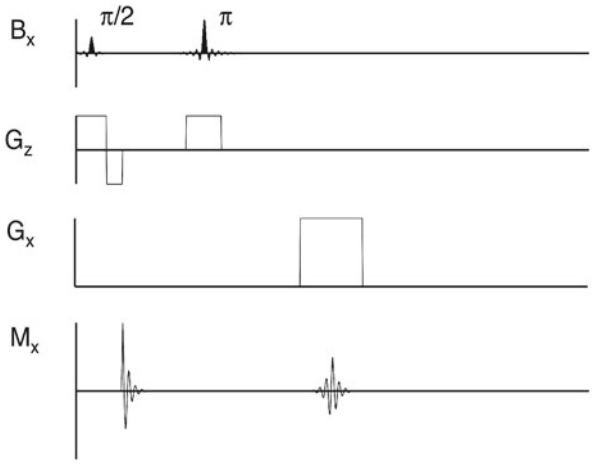

Fig. 18.26 A gradient G_x is applied during x readout. The echo signal between ω and $\omega + d\omega$ is proportional to the magnetization in a strip between x and $x + dx$, integrated over all values of y

The voltage induced in the pickup coil surrounding the sample is proportional to the free induction decay of **M** in the entire slice. That is, the voltage signal induced in the pickup coil is proportional to $\int M(x, y, z) \cos(-\omega_0 t) f(t)\, dV$, where $M(x, y, z)$ is the magnetization per unit volume that was nutated into the xy plane, $\cos(-\omega_0 t)$ represents the change in signal as **M** rotates in the xy plane at the Larmor frequency, and $f(t)$ represents relaxation, signal buildup during an echo, and so on. Figure 18.24 shows the echo after a subsequent π pulse, applied with G_z on, and which also has the form of a sinc function to affect only those spins in the slice of interest.

We assume that changes in $f(t)$ are slow compared to the Larmor frequency and neglect them here. Then the signal from an element $dxdy$ in the slice is

$$v(t) = A\, dx\, dy\, \Delta z\, M(x, y, z) \cos(-\omega_0 t). \tag{18.43}$$

Constant A includes all the details of the detecting coils and receiver.

18.9.2 Readout in the Direction

We now need to extract x and y position information from $v(t)$. This is done by creating gradients of B_z in the x or y directions. As shown in Fig. 18.25, if the signal is measured while a gradient is applied, the Larmor frequency varies with position. Suppose that B_z is given a gradient G_x in the x direction during the echo signal readout, as shown in Fig. 18.26. G_x is called the *readout* or *frequency encoding* gradient. The spins that echo in the shaded slice between x and $x + dx$ in Fig. 18.27 will be precessing with a Larmor frequency between ω and $\omega + d\omega$, where $\omega = \omega_0 + \gamma G_x x$.

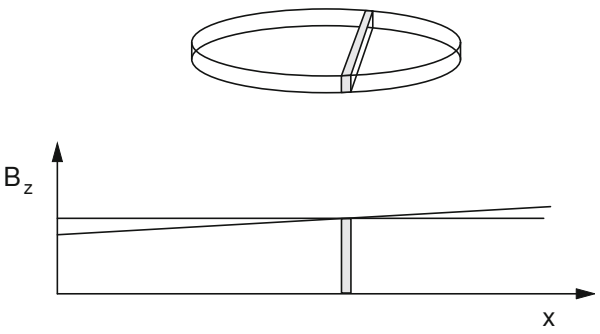

Fig. 18.27 Because the gradient G_x is applied during readout, the Larmor frequency of all spins in the shaded slice is between ω and $\omega + d\omega$

The signal from the entire slice is

$$v(t) = A\Delta z \int dx \left(\int dy\, M(x, y, z) \right) \cos[-\omega(x)t]. \tag{18.44}$$

We use the fact that $\omega(x) = \omega_0 + \gamma G_x x$ to write the signal as

$$v(t) = A\Delta z \int dx \left[\left(\int dy\, M(x, y, z) \right) \cos(-\omega_0 t - \gamma G_x x t) \right]. \tag{18.45}$$

Since the z slice has already been selected, let us simplify the notation by dropping the z dependence of **M**. The electronics in the detector multiply $v(t)$ by $\cos(\omega_0 t)$ or $\sin(\omega_0 t)$ and average over many cycles at the Larmor frequency.

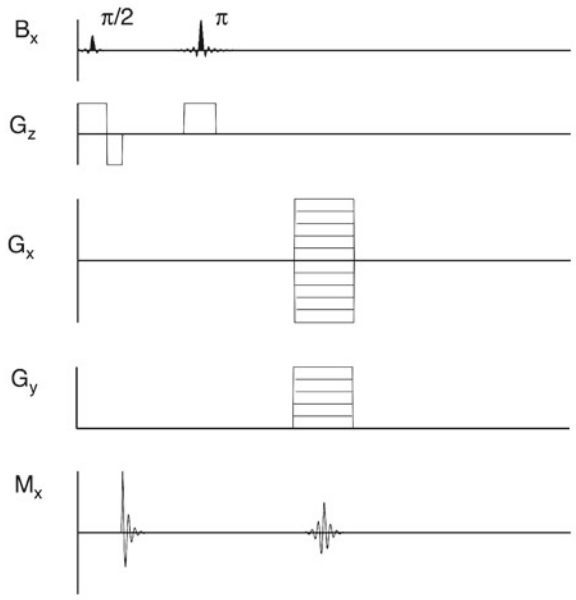

Fig. 18.28 Projection reconstruction techniques can be used to form an image. A series of measurements are taken, each with simultaneous gradients G_x and G_y

The results are two signals that form the basis for constructing the image:

$$s_c(t) = \overline{v(t)\cos(\omega_0 t)} \propto \iint dx\,dy\,M(x,y)\cos(-\gamma G_x x t),$$
$$s_s(t) = \overline{v(t)\sin(\omega_0 t)} \propto \iint dx\,dy\,M(x,y)\sin(-\gamma G_x x t). \tag{18.46}$$

The time average is over many cycles at the Larmor frequency but a time short compared to $2\pi/\gamma G_x x_{\max}$.

18.9.3 Projection Reconstruction

By inspecting Eq. 18.46 and remembering the relationship between ω and x, we see that the Fourier transforms of $s_c(t)$ and $s_s(t)$ are both proportional to $\int M(x,y)\,dy$. (Of course, the signals are digitized and one actually deals with discrete transforms.) This means that s_c or s_s can be Fourier analyzed to determine the amount of signal in the frequency interval $(\omega, d\omega)$ corresponding to (x, dx), which is proportional to the projection $\int M(x,y)\,dy$ along the shaded strip. In Sect. 12.5 we learned how to reconstruct an image from a set of projections. The entire readout process can therefore be repeated with the gradient rotated slightly in the xy plane (that is, with a combination of G_x and G_y during readout). This is indicated in Fig. 18.28, which indicates many scans, with different values of G_x and G_y, related by $G_y/G_x = \tan\theta$, where θ is the angle between the projection and the x axis. All of the techniques for reconstruction from projections that were developed for computed tomography can be used to reconstruct $M(x,y)$. Sending the proper combination of currents through the x and y gradient coils rotates the gradient; no rotating mechanical components are needed.

18.9.4 Phase Encoding

Techniques are available for magnetic resonance imaging that are not available for computed tomography. They are based on determining directly the Fourier coefficients in two or three dimensions. The basic technique is called *spin warp* or *phase encoding*. We saw in Fig. 18.25 that if a gradient is applied after the $\pi/2$ slice-selection pulse, a position-dependent phase shift remains even after the gradient is turned off. Let us make this quantitative. We wish to construct an image of $M(x,y)$, modified by the function $f(t)$ that accounts for relaxation, etc. For simplicity of notation we again assume f is unity and suppress the z dependence, since slice selection has already been done. We will construct $M(x,y)$ from its Fourier transform. The Fourier transform of $M(x,y)$ is given by Eqs. 12.9:

$$M(x,y) = \left(\frac{1}{2\pi}\right)^2 \int_{-\infty}^{\infty} dk_x \int_{-\infty}^{\infty} dk_y [C(k_x,k_y)\cos(k_x x + k_y y) + S(k_x,k_y)\sin(k_x x + k_y y)]. \tag{18.47a}$$

with the coefficients given by

$$C(k_x,k_y) = \int_{-\infty}^{\infty} dx \int_{-\infty}^{\infty} dy\,M(x,y)\cos(k_x x + k_y y), \tag{18.47b}$$

$$S(k_x,k_y) = \int_{-\infty}^{\infty} dx \int_{-\infty}^{\infty} dy\,M(x,y)\sin(k_x x + k_y y). \tag{18.47c}$$

Our problem is to determine C and S and from them construct the image.

The information from the x readout gives us $C(k_x,0)$ and $S(k_x,0)$ directly. We show this for the cosine transform. From Eq. 18.47b

$$C(k_x,0) = \int_{-\infty}^{\infty} dx \left(\int_{-\infty}^{\infty} dy\,M(x,y)\right)\cos(k_x x). \tag{18.48}$$

Comparing this to the expression for $s_c(t)$ in Eq. 18.46, we see that

$$C(k_x,0) \propto s_c(k_x/\gamma G_x). \tag{18.49a}$$

Similarly,

$$S(k_x,0) \propto s_s(k_x/\gamma G_x). \tag{18.49b}$$

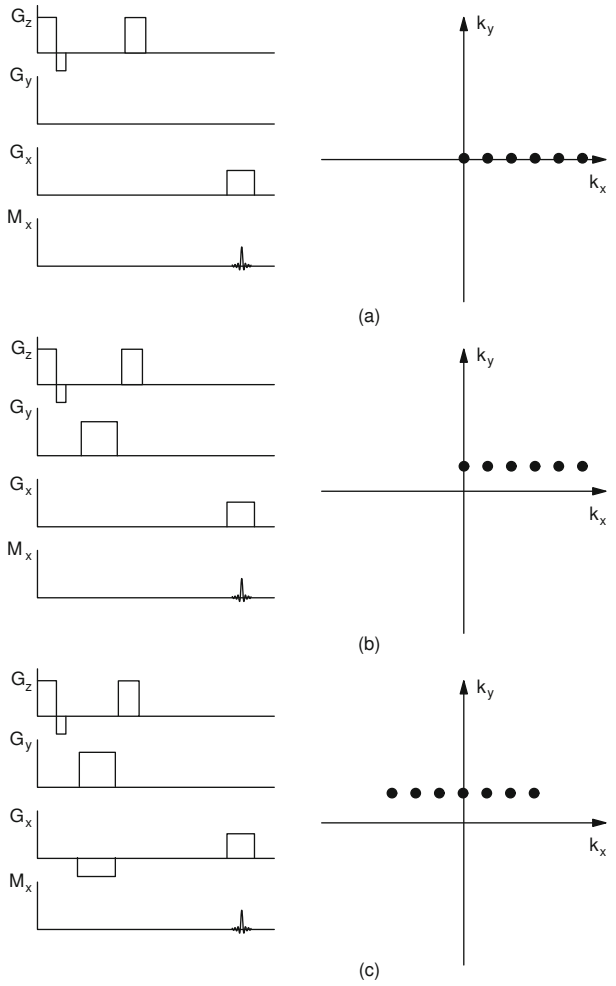

Fig. 18.29 **a** The signal measured while the x gradient is applied gives the spatial Fourier transform of the image along the k_x axis. **b** The addition of a phase-encoding gradient sets a nonzero value for k_y so that the readout determines the spatial Fourier transform along a line parallel to the k_x axis. **c** Phase encoding along the x axis as well shifts the line along which the coefficients are determined

The times at which s_c and s_s are measured and therefore the values of k_x are, of course, discrete. The discussion in Sect. 12.3 shows that the values of k_x are multiples of the lowest spatial frequency: $k_x = m\,\Delta k = mk_0 = 2\pi m/L_x$. The corresponding times to measure the signal are $t_m = 2\pi m/L_x\gamma G_x$. The spatial extent of the image in the x direction or *field of view* L_x determines the spacing Δk_x. The desired pixel size determines the maximum value of k_x or m: $\Delta x = \pi/k_{\max} = L_x/2m_{\max}$. The discrete values of k_x are shown in Fig. 18.29a.

The next problem is to make a similar determination for nonzero values of k_y. To do so, a gradient $G_y = \partial B_z/\partial y$ is applied at some time between slice selection and readout. This makes the Larmor frequency vary in the y direction. If the phase-encoding pulse is due to a uniform gradient that

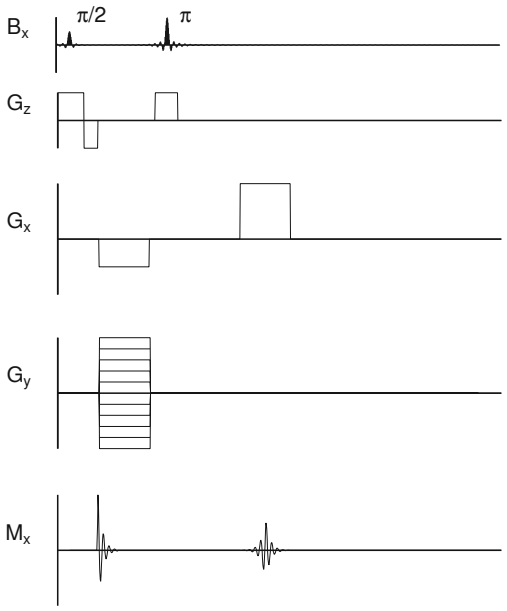

Fig. 18.30 The signals in a standard phase encoding. The pulse sequence is repeated for each value of k_y

lasts for a time T_p, the total phase change is

$$\Delta\phi = \int \omega(t)\,dt = \gamma G_y T_p y = k_y y. \tag{18.50}$$

The readout signal, Eq. 18.44, is replaced by

$$v(t) = A\,\Delta z \int dx \int dy\, M(x, y)\cos[\omega(x)t + k_y y]. \tag{18.51}$$

Note that the added phase does not depend on t because G_y is not on during readout. However, the cosine term must now be included in both the x and y integrals. Carrying through the mathematics of the detection process shows that temporal Fourier transformation of the signals determines $C(k_x, k_y)$ and $S(k_x, k_y)$ for all values of k_x and for the particular value of k_y determined by the G_y phase selection pulse. Different values of the G_y pulse give the coefficients for different values of k_y, as shown in Fig. 18.29. Both positive and negative gradients are used to give both positive and negative values of k_y. Application of a gradient G_x during the phase-encoding time (in addition to the readout gradient) changes the starting value of k_x. This allows one to determine the coefficients for negative values of k_x. This figure has been drawn without taking into account that the application of a π pulse changes k_x to $-k_x$ and k_y to $-k_y$. The gradients and signals for this spin-echo determination are shown in Fig. 18.30. The coefficients are substituted in Eq. 18.47a to reconstruct $M(x, y, z)$ for the z slice in question.

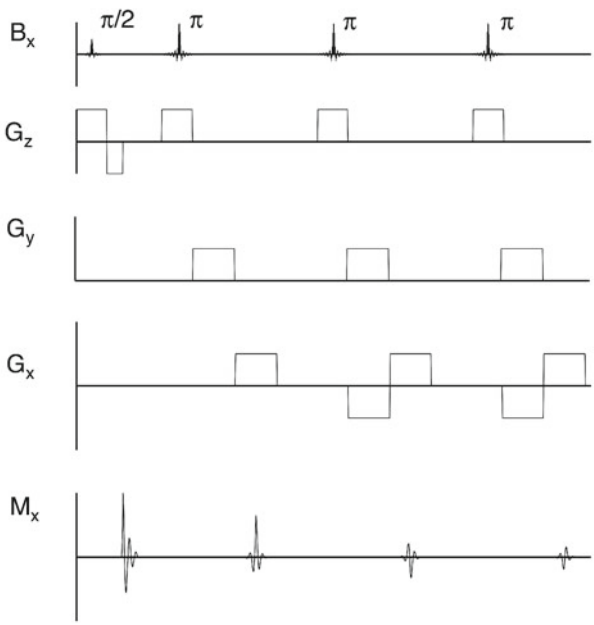

Fig. 18.31 A fast spin-echo sequence uses a single $\pi/2$ slice selection pulse followed by multiple echo rephasing pulses. A correction must be made for the transverse decay

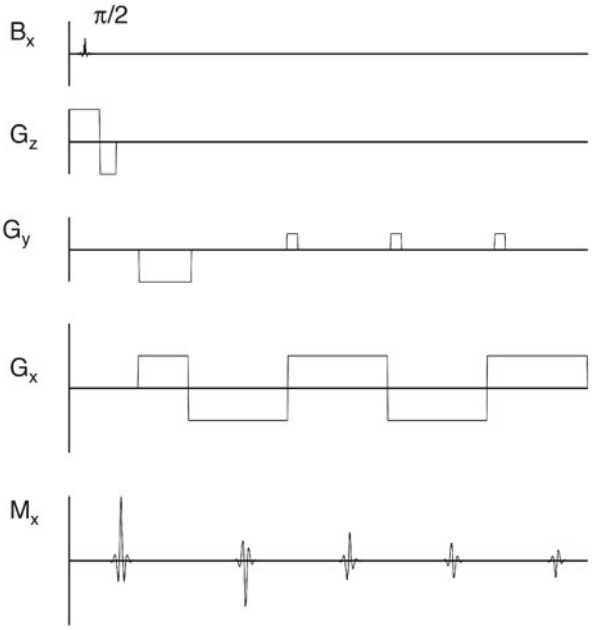

Fig. 18.32 Echo planar imaging uses a very uniform magnet and eliminates the rephasing π pulses. In Fig. 18.31 the decay of the individual echoes was determined by T_2^*, and the slower decay of the amplitude of the subsequent echoes was determined by T_2. In this figure the decay of the individual echoes is determined by the size of the gradient and the slower decay of the amplitude of the subsequent echoes is determined by T_2^*

18.9.5 Other Pulse Sequences

Dozens of other pulse sequences have been invented, all of which are based on the fundamentals presented here. We mention only a few, and there are many variations of these. For details, see Bernstein et al. (2004).

Fast spin echo or *turbo spin echo* uses a single $\pi/2$ pulse, followed by a series of π pulses, as shown in Fig. 18.31. Each π pulse produces an echo, though the echo amplitudes decay and a correction for this must be made in the image reconstruction. Each G_y pulse increments or *winds* the phase by a fixed amount. A negative G_x pulse resets the positions of the k_x values. Faster image acquisition sequences not only save time, but they may allow the image to be obtained while the patient's breath is held, thereby eliminating motion artifacts.

The major problem with conventional spin echo (Fig. 18.30) is that one must wait a time $T_R \gg T_1$ between measurements for different values of k_y. One way to speed things up is to use the intervening time to make measurements in a slice at a different value of z. Another technique is to use a flip angle smaller than $\pi/2$. Suppose the flip angle is $\alpha = 20\,^\circ$. This gives a transverse magnetization proportional to $\sin 20\,^\circ = 0.34$ while reducing the longitudinal magnetization only slightly, to $\cos 20\,^\circ = 0.94$. Thus, k space can be sampled until the transverse signal has decayed and another α flip pulse can immediately be applied to restore the transverse magnetization.

Echo-planar imaging (EPI) eliminates the π pulses. It requires a magnet with a very uniform magnetic field, so that T_2 (in the absence of a gradient) is only slightly greater than T_2^*. The gradient fields are larger, and the gradient pulse durations shorter, than in conventional imaging. The goal is to complete all the k-space measurements in a time comparable to T_2^*. In EPI the echoes are not created using π pulses. Instead, they are created by dephasing the spins at different positions along the x axis using a G_x gradient, and then reversing that gradient to rephase the spins, as shown in Fig. 18.32. Whenever the integral of $G_x(t)$ is zero, the spins are all in phase and the signal appears. A large negative G_y pulse sets the initial value of k_y to be negative; small positive G_y pulses ("blips") then increase the value of k_y for each successive k_x readout. Echo-planar imaging requires strong gradients—at least five times those for normal studies—so that the data can be acquired quickly. Moreover, the rise- and fall-times of these pulses are short, which induces large voltages in the coils. Eddy currents are also induced in the patient, and it is necessary to keep these below the threshold for neural activation. These problems can be reduced by using sinusoidally-varying gradient currents. The engineering problems are discussed in Schmitt et al. (1998); in Vlaardingerbroek and den Boer (2004); and in Bernsteinet al. (2004).

High spatial frequencies give the sharp edge detail in an image; the lowest spatial frequencies give the overall contrast. (We saw this in Figs. 12.9 and 12.10.) Changing the order of sampling points in k space can be useful. For example, when the image may be distorted by blood flow (see Sect. 18.11), it is possible to change the gradients in such a way that the values of k near zero are measured right after the excitation. This gives the proper signal within the volume of the vessel. The higher spatial frequencies, which show vessel edges, are less sensitive to blood flow and are acquired later.

A three-dimensional Fourier transform of the image can be obtained by selecting the entire sample and then phase encoding in both the y and z directions while doing frequency readout along x. One must step through all values of k_y for each value of k_z. This is one way to image very small samples with very high resolution (MRI microscopy) (Callaghan 1994).

18.9.6 Image Contrast and the Pulse Parameters

The appearance of an MR image can be changed drastically by adjusting the repetition time and the echo time. Problem 27 derives a general expression for the amplitude of the echo signal when a series of $\pi/2$ pulses are repeated every T_R seconds. The magnetic moment in the sample at the time of the measurement, considering both longitudinal and transverse relaxation, is

$$M(T_R, T_E) \tag{18.52}$$
$$= M_0 \left(1 - 2e^{-T_R/T_1 + T_E/2T_1} + e^{-T_R/T_1}\right) e^{-T_E/T_2},$$

where M_0 is proportional to the number of proton spins per unit volume N, as shown in Eq. 18.10. If $T_R \gg T_E$, this simplifies to

$$M(T_R, T_E) = M_0(1 - e^{-T_R/T_1})e^{-T_E/T_2}, \tag{18.53}$$

We consider an example that compares muscle ($M_0 = 1.02$ in arbitrary units, $T_1 = 500$ ms, and $T_2 = 35$ ms) with fat ($M_0 = 1.24$, $T_1 = 200$ ms, and $T_2 = 60$ ms).

Figure 18.33 shows two examples where T_R is relatively long and M_0 returns nearly to its initial value between pulses. If the echo time is short, then the image is nearly independent of both T_1 and T_2 and it is called a *density-weighted image*. If T_E is longer, then the transverse decay term dominates and it is called a *T_2-weighted image*. The signal is often weak and therefore noisy because there has been so much decay.

Figure 18.34 shows what happens if the repetition time is made small compared to T_1. This is a *T_1-weighted image* because the differences in T_1 are responsible for most of the difference in signal intensity. Notice also that the very first pulse nutates the full M_0 into the transverse plane, so an echo after the first pulse would give an anomalous reading. Echoes are measured only for the second and later pulses.

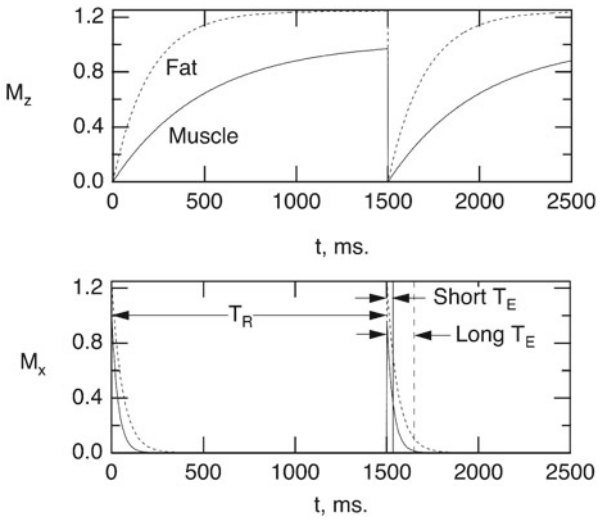

Fig. 18.33 The intensity of the signal from different tissues depends on the relationship between the repetition time and echo times of the pulse sequence, and the relaxation times of the tissues being imaged. This figure and the next show the magnetization curves for two tissues: muscle (relative proton density 1.02, $T_1 = 500$ ms, $T_2 = 35$ ms) and fat (relative proton density 1.24, $T_1 = 200$ ms, $T_2 = 60$ ms). The repetition time is 1500 ms, which is long compared to the longitudinal relaxation times. A long echo time gives an image density that is very sensitive to T_2 values. A short echo time (even shorter than shown) gives an image that depends primarily on the spin density

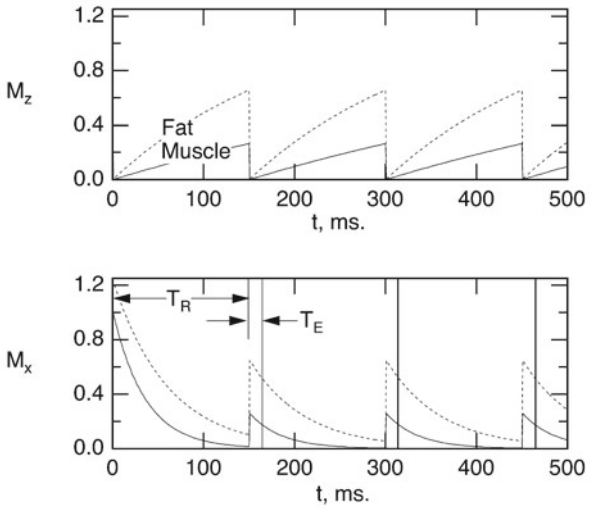

Fig. 18.34 The tissue parameters are the same as in Fig. 18.33. The repetition time is short compared to the longitudinal relaxation time. As a result, the first echo must be ignored. With a short T_E, the image density depends strongly on the value of T_1

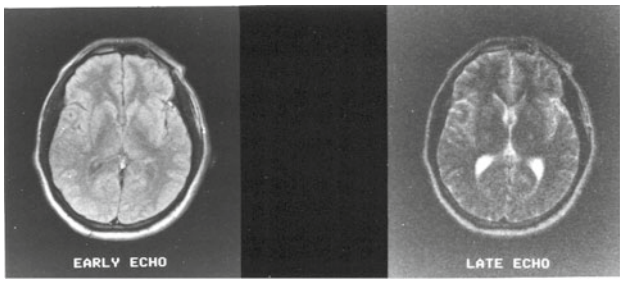

Fig. 18.35 Spin-echo images taken with short and long values of T_E, showing the difference in T_2 values for different parts of the brain. (Photograph courtesy of R. Morin, Ph.D., Department of Diagnostic Radiology, University of Minnesota)

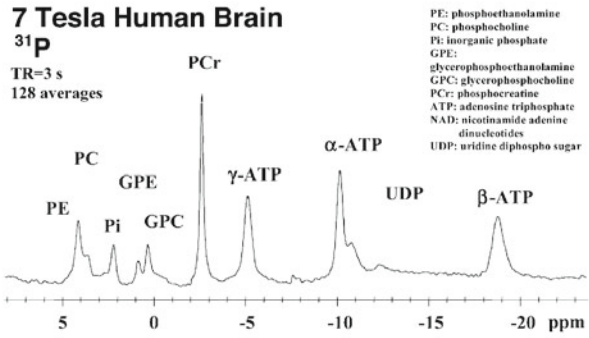

Fig. 18.36 A chemical shift spectrum for ^{31}P taken from the visual cortex at the back of the brain using a 7-tesla machine. (From Lei et al. 2003. Used by permission. Image courtesy of Prof. Kamil Ugurbil)

Suppose that the value of T_2 for fat had been shorter than the value for muscle. Then there would have been a value of T_E for which the two transverse magnetization curves crossed, and the two tissues would have been indistinguishable in the image. At larger values of T_E, their relative brightnesses would have been reversed. Figure 18.35 shows spin-echo images taken with two different values of T_E, for which the relative brightnesses are quite different.

18.9.7 Safety

Safety issues in MRI include forces on magnetic objects in and around the patient such as aneurysm clips, hairpins, pacemakers, wheel chairs, and gas cylinders (Kanal et al. 2007), absorbed radio-frequency energy (Problem 21), and induced currents from rapidly-changing magnetic field gradients. The rapid changes of magnetic field can stimulate nerves and muscles, cause heating in electrical leads and certain tattoos, and possibly induce ventricular fibrillation. Induced fields are reviewed by Schaefer et al. (2000). Cardiac pacemakers are being designed to be immune to the strong—and rapidly varying—magnetic and rf fields (Santini et al. 2013).

18.10 Chemical Shift

If the external magnetic field is very homogeneous, it is possible to detect a shift of the Larmor frequency due to a reduction of the magnetic field at the nucleus because of diamagnetic shielding by the surrounding electron cloud. The modified Larmor frequency can be written as

$$\omega = \gamma B_0(1 - \sigma). \tag{18.54}$$

Typical values of σ are in the range 10^{-5} to 10^{-6}. They are independent of B_0, as expected for a diamagnetic effect proportional to B_0. Measurements are made by Fourier transformation of the free-induction-decay signal, averaged over many repetitions if necessary to provide the resolution required to detect the shift.

A great deal of work has been done with ^{31}P, because of its presence in adenosine triphosphate and adenosine diphosphate (ATP and ADP). Free energy is supplied for many processes in the body by the conversion of ATP to ADP. Fig. 18.36 shows a very high resolution chemical shift spectrum from the human visual cortex taken with a 7-tesla machine.

It is also possible to make chemical shift images. Figure 18.37 shows a series of ^{31}P spectra from the brain. An image of the slice from which these data are obtained is shown below the spectra. The slice on the left cuts through the cerebellum and temporal lobes of the brain. It also includes some skeletal muscle. The slice on the right is through brain only.

18.11 Flow Effects

Flow effects can distort a magnetic resonance image. Spins initially prepared with one value of **M** can flow out of a slice before the echo and be replaced by spins that had a different initial value of **M**. This is called *washout*. Spins that have been shifted in phase by a field gradient can flow to another location before the readout pulse is applied. This causes artifacts and can also be used to measure blood flow (Axel 1984; Battocletti et al. 1981).

To understand the washout effect consider a simple model in which a blood vessel is perpendicular to the slice, as shown in Fig. 18.38. To simplify further, assume that all the blood

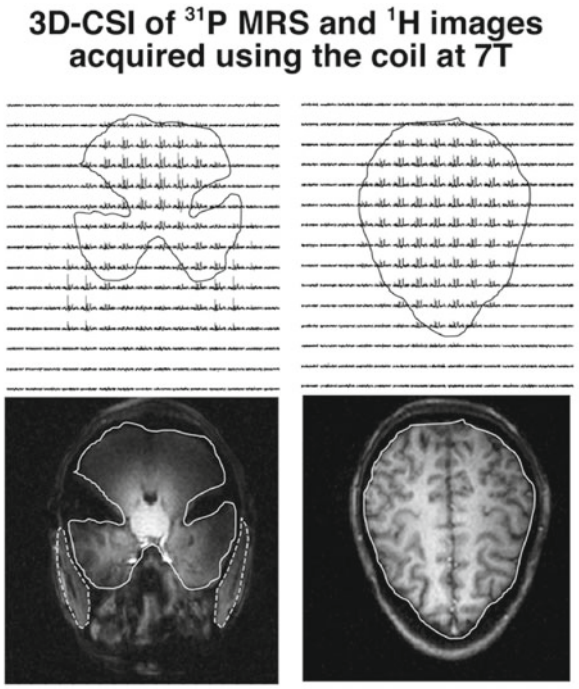

Fig. 18.37 The image on the left displays ^{31}P chemical shift data as spectra from individual voxels. The image of the slice from which these data are obtained is shown below the spectra. The slice cuts through the cerebellum and temporal lobes of the brain (solid outline). The dashed lines mark skeletal muscle which also contains phosphorylated metabolites, with a higher creatine phosphate level (PCr) compared to brain. The slice on the right is through the brain only. (Image courtesy of Prof. Kamil Ugurbil, University of Minnesota)

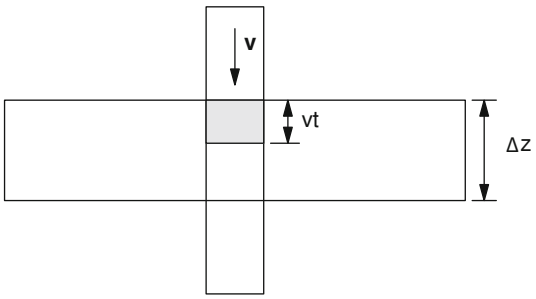

Fig. 18.38 A blood vessel is perpendicular to the slice. The model developed in the text assumes plug flow, that is, all of the blood is flowing with the same speed v

flows with the same speed v, independent of where it is in the vessel. This is called *plug flow*.

First consider washout of the excited spins. Suppose that at time $T_E/2$ a π pulse is applied to the slice in Fig. 18.38 and that the echo is measured at time T_E. The shaded area in the vessel represents new blood that flows in during time t. If the flow velocity is zero, no new blood flows in, all of the blood in the slice was excited, and the signal has full strength. If the velocity is greater than $2\Delta z/T_E$, all of the spins that were flipped by the pulse will leave the sensitive region by the time of the echo, and there will be no signal. Because we assume plug flow, the fraction washed out is a linear function of velocity up to the critical value of v. The fraction of excited spins remaining at T_E is given by

$$f = \begin{cases} 1 - \dfrac{vT_E}{2\Delta z}, & v < 2\Delta z/T_E \\ 0, & v \geq 2\Delta z/T_E. \end{cases} \tag{18.55}$$

Now consider washout of spins between pulses. We saw that the effect of repetition and echo times on the MRI signal is given by Eq. 18.52, which, if $T_R \gg T_E$, simplifies to Eq. 18.53. For low velocities ($v < \Delta z/T_R$) there is an enhancement of the signal because blood with a larger value of M_z flows into the sensitive region. For $vT_R < \Delta z$, the factor in parentheses in Eq. 18.53 is replaced by

$$\frac{vT_R}{\Delta z} + \left(1 - \frac{vT_R}{\Delta z}\right)\left(1 - e^{-T_R/T_1}\right).$$

The first term represents spins that flow in and the second those that still remain and that are still affected by the previous pulse. This can be rearranged as

$$\left(1 - e^{-T_R/T_1}\right) + \frac{vT_R}{\Delta z} e^{-T_R/T_1}. \tag{18.56}$$

This factor has the value $1 - e^{-T_R/T_1}$ for small v and is proportional to v when $v \gg \Delta z/T_R$. More complicated models can be developed. Phase changes because the blood flows through magnetic field gradients are also important.

Blood perfusion in the brain can be monitored using *arterial spin labeling* (Wolf and Detre 2007). A π pulse inverts the spins in a slice just upstream of the region of interest. Blood flow carries these labeled spins into the slice to be imaged. A second image of the slice is acquired without labeling the spins. The difference between the two images provides information about perfusion.

In addition to blood flow, MRI can also be used to image motion of the tissue. In *magnetic resonance elastography*, an acoustic signal is applied to the tissue (typically 0.1-1 kHz), creating a shear wave (Chap. 13). A magnetic resonance image is then obtained, using a magnetic field gradient that oscillates at the same frequency as the acoustic wave. In stationary tissue, the positive and negative phases produced by an oscillating gradient cancel to produce no net phase change, but in the oscillating tissue the phase shifts accumulate. Thus, information about the amplitude of the tissue motion is encoded in the phase of the magnetic resonance signal. When the applied signal and tissue response are both known, the shear modulus (Chap. 1) can be determined. If, for instance, a tumor is stiffer than the surrounding tissue, it will be imaged as a region of high shear modulus (Mariappan et al. 2010).

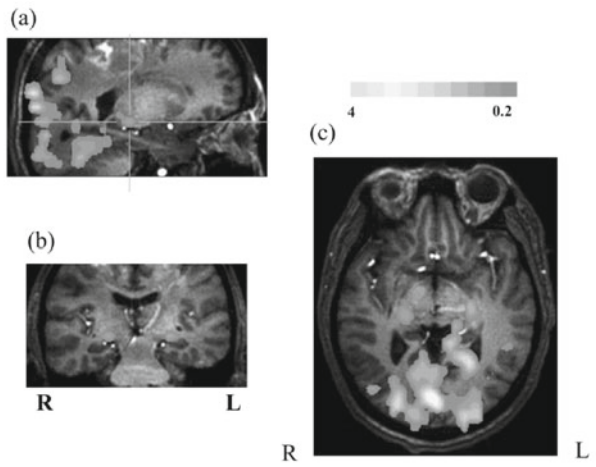

Fig. 18.39 Functional MRI in three planes: **a** sagittal (side) view; **b** coronal (front) view; **c** axial view (from below). The layers viewed in **b** and **c** are indicated by the lines in **a**. Bright spots superimposed on the image show activity in the visual cortex and in some structures between the eye and the visual cortex. The magnetic field is 4 T. (Adapted from Chen et al. 1998. Image supplied by Prof. Kamil Ugurbil)

18.12 Functional MRI

Magnetic resonance imaging provides excellent structural information. Various contrast agents can provide information about physiologic function. For example, contrast agents containing gadolinium are injected intravenously (Hao et al. 2012). They leak through a damaged blood-tissue barrier and accumulate in the damaged region. At small concentrations T_1 is shortened. One can also inject a contrast agent and watch its first pass through the circulatory system. Such an agent typically changes the magnetic susceptibility and shortens T_2.

The term *functional magnetic resonance imaging* (fMRI) usually refers to a technique developed in the 1990s that allows one to study structure and function simultaneously. The basis for fMRI is inhomogeneities in the magnetic field caused by the differences in the magnetic properties of oxygenated and deoxygenated hemoglobin. No external contrast agent is required. Oxygenated hemoglobin is less paramagnetic than deoxyhemoglobin. If we make images before and after a change in the blood flow to a small region of tissue (perhaps caused by a change in its metabolic activity), the difference between the two images is due mainly to changes in the blood oxygenation. One usually sees an increase in blood flow to a region of the brain when that region is active. This BOLD contrast in the two images provides information about the metabolic state of the tissue, and therefore about the tissue function (Ogawa et al. 1990; Kwong et al. 1992).

An image of the brain during visual stimulation is shown in Fig. 18.39. In addition to the visual cortex in part c, activity is seen in the lateral geniculate nucleus (parts b and c), which is on the pathway from the eye to the visual cortex. Functional MRI provides functional information similar to that from PET (Sect. 17.10), but without the need for radionuclides.

Other contrast agents, usually a complex molecule shielding a gadolinium atom, are being developed to measure pH, ions such as zinc, calcium, and copper, and certain enzymes (Louie 2013). The stable isotope ^{19}F is being tested as an alternative to gadolinium (Ahrens and Zhong 2013).

Another recent technique that can be classified as functional is the detection of prostate cancer that has metastasized to a lymph node when the metastasis is not yet apparent by other imaging techniques. Monocrystalline iron oxide particles injected in the blood will be taken up by normal lymph nodes but not those with metastases. The technique is effective for lymph nodes larger than 5 mm (Harisinghani et al. 2003; see also the commentary by Koh et al. 2003).

Much recent research has focused on using MRI to image neural activity directly, rather than through changes in blood flow (Bandettini et al. 2005). Two methods have been proposed to do this. In one, the biomagnetic field produced by neural activity (Chap. 8) acts as the contrast agent, perturbing the magnetic resonance signal. Images with and without the biomagnetic field present provide information about the distribution of neural action currents. In an alternative method, the Lorentz force (Eq. 8.2) acting on the action currents in the presence of a magnetic field causes the nerve to move slightly. If a magnetic field gradient is also present, the nerve may move into a region having a different Larmor frequency. Again, images taken with and without the action currents present provide information about neural activity. Unfortunately, both the biomagnetic field and the displacement caused by the Lorentz force are tiny, and neither of these methods has yet proved useful for neural imaging. However, if these methods could be developed, they would provide information about brain activity similar to that from the magnetoencephalogram, but without requiring the solution of an ill-posed inverse problem that makes the MEG so difficult to interpret.

18.13 Diffusion and Diffusion Tensor MRI

Our analysis of MRI so far assumes that the nuclei are stationary except for the rotation of their spin axis or their motion with the blood to create flow effects. In practice, these nuclei are also free to diffuse throughout the tissue (Chap. 4). The magnetization $\mathbf{M}$ depends on the total number of particles per unit volume with average spin components $\langle \mu_x \rangle$,

$\langle \mu_y \rangle$, and $\langle \mu_z \rangle$. In the rotating coordinate system there is no precession. In the absence of relaxation effects $\langle \boldsymbol{\mu} \rangle$ does not change. In that case changes in $\mathbf{M}$ depend on changes in the concentration of particles with particular components of $\langle \boldsymbol{\mu} \rangle$, so the rate of change of each component of $\langle \boldsymbol{\mu} \rangle$ is given by a diffusion equation. For example, for M_x,

$$\frac{\partial M_x}{\partial t} = D\nabla^2 M_x.$$

If the processes are linear, this diffusion term can be added to the other terms in the Bloch equations. The details are explored in Problem 47.

In a spin–echo pulse sequence, the amplitude of the echo will be smaller if the spins have diffused to different locations within the tissue between the time of the excitation pulse and the echo. This artifact degrades the signal during traditional MRI, but can be valuable if one wants to measure the diffusion constant. The rate of diffusion depends sensitively on temperature, so measurements of the diffusion constant provide a way to monitor internal temperatures noninvasively (Delannoy et al. 1991). Moseley et al. (1990) showed that diffusion MRI is valuable for detecting regional cerebral ischemia, and it has become a useful tool in stroke research.

Diffusion can be monitored during a spin-echo sequence by applying magnetic field gradients of the same magnitude and duration before and after the π pulse, as shown in Fig. 18.40. If a spin is stationary, these gradients have no effect: they shift the phase of the spins in one direction before the π pulse, but shift the phase in the other direction after the π pulse, restoring the original phase. However, for spins that diffuse from one location to another between the application of the gradients, the phase shift of the first gradient is not cancelled by an opposite phase shift in the second, so the gradients introduce a net phase shift. This shift lowers the echo amplitude, with the reduction depending on the square of the gradient and the diffusion constant (Prob. 47).

In some tissues diffusion is anisotropic, meaning that the diffusion constant depends on direction. In such cases the effect of diffusion depends on the direction of the magnetic field gradient. Basser et al. (1994) extended diffusion MRI so that the entire diffusion tensor is measured. The diffusion tensor (or matrix) is similar to the conductivity tensor discussed in Sect. 7.9. Using matrix notation, the fluence rate of diffusing particles with aligned nuclear spins is related to the particle concentration by

$$\begin{pmatrix} j_x \\ j_y \\ j_z \end{pmatrix} = - \begin{pmatrix} D_{xx} & D_{xy} & D_{xz} \\ D_{yx} & D_{yy} & D_{yz} \\ D_{zx} & D_{zy} & D_{zz} \end{pmatrix} \begin{pmatrix} \dfrac{\partial C}{\partial x} \\ \dfrac{\partial C}{\partial y} \\ \dfrac{\partial C}{\partial z} \end{pmatrix}. \qquad (18.57)$$

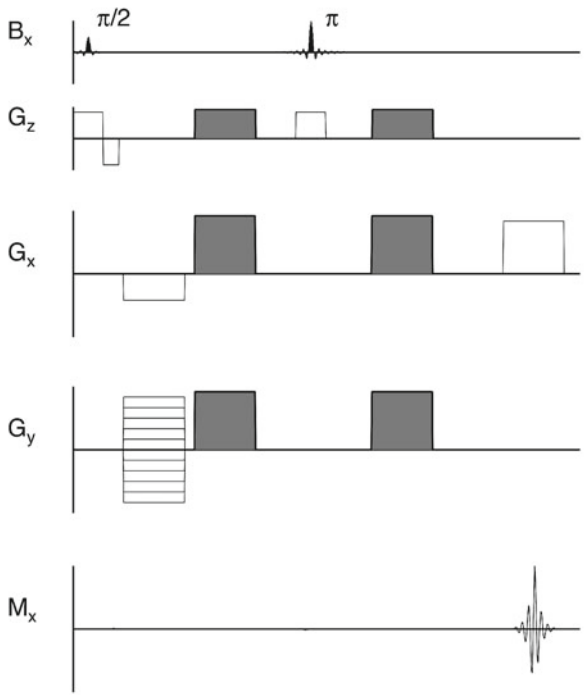

Fig. 18.40 A silmplified pulse sequence for diffusion tensor imaging. The sequence is similar to that shown in Fig. 18.30 for two-dimensional imaging using phase encoding. The M_x signal is shown only during readout. The diffusion gradients, shown in gray, are applied before and after the π pulse. For stationary spins, any phase shift produced by the first diffusion gradient is canceled by an opposite phase shift produced by the second diffusion gradient. Spins that diffuse during this pulse sequence are affected differently by the first and second diffusion gradients, which affects the signal. For diffusion tensor imaging the gradients must be applied in all three directions. For more details, see Mattiello et al. (1994)

One can show that the diffusion matrix is always symmetric: $D_{yx} = D_{xy}$, etc.

Diffusion is usually greater along the direction of the nerve or muscle fibers. Since the orientation of the fibers changes throughout the body, the elements of the diffusion tensor vary as well. However, some features of the diffusion tensor, such as the trace (see Prob. 49), are independent of the fiber direction, and are particularly useful when monitoring diffusion in anisotropic tissue, such as the white matter of the brain. In addition, the diffusion tensor contains information about the fiber direction, allowing one to map fiber tract trajectories noninvasively using MRI (Basser et al. 2000). See also the review by Thomas et al. (2000).

18.14 Hyperpolarized MRI of the Lung

The lung is difficult to image using MRI because of its low proton density. A new way to monitor lung function is to image the isotope ^{129}Xe inhaled into the lungs. The density

of ^{129}Xe is small, but the magnetization can be increased dramatically using the technique of *hyperpolarization* (Mugler and Altes 2013). In this two-step process, a laser is used to generate electron-spin polarization in a vapor of alkali metal such as rubidium subject to a magnetic field. Then collisions with the rubidium molecules transfer the polarization to the ^{129}Xe. This technique increases the polarization by a factor of about 1000 beyond what it would be in thermal equilibrium.

Symbols Used in Chapter 18

Symbol	Use	Units	First used page
a	Loop radius	m	545
a, b	Constants	J T^{-1} m^{-3}	541
f	Fraction		556
h	Planck's constant	J s	542
$\hbar$	Planck's constant (reduced)	J s	537
i	Current	A	536
j_x, j_y, j_z	fluence rate	m^{-2} s^{-1}	558
k_B	Boltzmann constant	J K^{-1}	537
k_x, k_y, k_z	Spatial frequency	m^{-1}	551
m	Mass	kg	537
m	Azimuthal quantum number		537
m	Integer		552
q	Electric charge	C	537
r	Radius	m	537
s	Signal	V	551
t	Time	s	536
v	Velocity	m s^{-1}	537
v	Voltage difference	V	544
x	Dimensionless variable		549
x, y, z	Axes	m	538
x', y', z'	Axes (rotating)	m	540
Δz	Slice thickness	m	549
A	Amplitude	T s	550
A	Constant	V T J^{-1}	550
B, $\mathbf{B}$	Magnetic field	T	535
B_1	Oscillating magnetic field	T	540
C	Constant in expression for relaxation time	s^{-2}	543
$C(k), S(k)$	Fourier transforms	J T^{-1} m^{-1}	551
C	Concentration	m^{-3}	558
D_{xx}, etc.	Components of diffusion tensor	m^2 s^{-1}	558
E	Energy	J	542
G_x, G_y, G_z	Gradient of B_z in the x, y, or z direction	T m^{-1}	549
$\mathbf{I}$	Nuclear angular momentum	kg m^2 s^{-1}	537
I	Nuclear angular momentum quantum number		537
K	Constant		544
L, $\mathbf{L}$	Orbital angular momentum	kg m^2 s^{-1}	536
M, $\mathbf{M}$	Magnetization	J T^{-1} m^{-3}	537
N	Number of spins per unit volume	m^{-3}	537
$\mathbf{R}$	Rotation matrix		540
S	Area	m^2	536
$\mathbf{S}$	Spin angular momentum	kg m^2 s^{-1}	537
T	Temperature	K	537
T	Period	s	541
T_E	Time of echo	s	547
T_I	Interrogation time	s	546
T_R	Repetition time between pulse sequences	s	548
T_1	Longitudinal relaxation time	s	538
T_2	Transverse relaxation time	s	538
T_2^*	Experimental transverse relaxation time	s	544
T_p	Length of gradient pulse	s	552
U	Potential energy	J	536
V	Volume	m^3	545
α	Arbitrary angle		542
γ	Gyromagnetic ratio	T^{-1} s^{-1}	536
μ, $\boldsymbol{\mu}$	Magnetic moment	J T^{-1}	535
μ_0	Magnetic permeability of space	T m A^{-1}	535
ν	Frequency	Hz	537
θ	Angle		536
σ	Chemical shift factor		555
τ, $\boldsymbol{\tau}$	Torque	N m	535
τ	Shift time for autocorrelation	s	543
τ_C	Correlation time	s	543
ω	Angular frequency	s^{-1}	537
ω_1	Angular frequency for B_1 rotation	s^{-1}	541
ω_0	Larmor angular frequency	s^{-1}	539
ϕ	Azimuthal angle		543
ϕ	Phase		552
ϕ_{11}	Autocorrelation function		543
Φ	Magnetic flux	weber (T m^2)	545
$\boldsymbol{\Omega}$	Angular velocity vector	s^{-1}	540

Problems

Section 18.1

Problem 1. Show that for a particle of mass m located at position $\mathbf{r}$ with respect to the origin, the torque about the origin is the rate of change of the angular momentum about the origin.

Section 18.2

Problem 2. Show that the units of γ are T^{-1} s^{-1}.

Problem 3. Find the ratio of the gyromagnetic ratio in Table 18.1 to the value $q/2m$ for the electron and proton.

Section 18.3

Problem 4. Evaluate the quantity $\gamma m\hbar B/k_B T$ and the Larmor frequency for electron spins and proton spins in magnetic fields of 0.5 and 4.0 T at body temperature (310 K).

Problem 5. Verify that $\sum 1 = 2I + 1$, $\sum m = 0$, and $\sum m^2 = I(I+1)(2I+1)/3$, when the sums are taken from $-I$ to I, in the cases that $I = \frac{1}{2}$, 1, and $\frac{3}{2}$.
Problem 6. Obtain an expression for the magnetization analogous to Eq. 18.10 in the case $I = \frac{1}{2}$ when one cannot make the assumption $\gamma\hbar B/k_B T \ll 1$.
Problem 7. Calculate the coefficient of B in Eq. 18.10 for a collection of hydrogen nuclei at 310 K when the number of hydrogen nuclei per unit volume is the same as in water.

Section 18.4

Problem 8. Verify that Eqs. 18.16 are a solution of Eqs. 18.15.
Problem 9. Calculate the value of $M_x^2 + M_y^2 + M_z^2$ for relaxation Eqs. 18.16 when $T_1 = T_2$.
Problem 10. Equations 18.16 correspond to a solution of the Bloch equations in the presence of a static field B for one initial condition: $M_x = M_0$, $M_y = 0$, $M_z = 0$. Solve the Bloch equations for a different initial condition: $M_x = 0$, $M_y = 0$, and $M_z = -M_0$.

Section 18.5

Problem 11. (a) Use Fig. 18.6 to derive Eq. 18.18.
(b) Show that

$$M_{x'} = M_x \cos\theta + M_y \sin\theta,$$

$$M_{y'} = -M_x \sin\theta + M_y \cos\theta.$$

(c) Combine these equations with the equations for M_x and M_y to show that the application of both transformations brings one back to the starting point.
Problem 12. Equation 18.17 shows how to transform the components of a vector in the primed system (rotated an angle θ clockwise from the unprimed system) into the unprimed system. Use the arguments of Section 18.5 to derive the following transformation matrices for counterclockwise rotations.
(a) Angle α about the x axis:

$$\begin{pmatrix} 1 & 0 & 0 \\ 0 & \cos\alpha & \sin\alpha \\ 0 & -\sin\alpha & \cos\alpha \end{pmatrix}$$

(b) Angle β about the y axis:

$$\begin{pmatrix} \cos\beta & 0 & -\sin\beta \\ 0 & 1 & 0 \\ \sin\beta & 0 & \cos\beta \end{pmatrix},$$

(c) Angle θ about the z axis:

$$\begin{pmatrix} \cos\theta & \sin\theta & 0 \\ -\sin\theta & \cos\theta & 0 \\ 0 & 0 & 1 \end{pmatrix}.$$

Why are the minus signs different from those in Eq. 18.17b?
Problem 13. Calculate $M^2 = M_x^2 + M_y^2 + M_z^2$ for the solution of Eqs. 18.30 and compare it to the results of Problem 9.

Section 18.6

Problem 14. Use Eqs. 18.32 to find the magnetic field at one proton due to the other proton in a water molecule when both proton spins are parallel to each other and perpendicular to the line between the protons. The two protons form an angle of 104.5° and are each 96.5×10^{-12} m from the oxygen.
Problem 15. The magnetic field at a distance of 0.15 nm from a proton is 4×10^{-4} T. What change in Larmor frequency does this ΔB cause? How long will it take for a phase difference of π radians to occur between a precessing spin feeling this extra field and one that is not?
Problem 16. Consider a collection of spins that are aligned along the x axis at $t = 0$. They precess in the xy plane with different angular frequencies spread uniformly between $\omega - \Delta\omega/2$ and $\omega + \Delta\omega/2$. If the total magnetic moment per unit volume is M_0 at $t = 0$, show that at time $T = 4/\Delta\omega$ it is $M_0 \sin(2)/2 = 0.455 M_0$.
Problem 17. What is the contribution to the transverse relaxation time for a magnetic field of 1.5 T with a uniformity of 1 ppm? The nonrecoverable relaxation time of brain is about 2.5 ms. What dominates the measured transverse relaxation in brain?
Problem 18. Suppose the two dipoles of the water molecule shown below point in the z direction while the line between them makes an angle θ with the x axis. Determine the angle θ for which the magnetic field of one dipole is perpendicular to the dipole moment of the other. For this angle the interaction energy is zero. This θ is called the *magic angle* and is used when studying anisotropic tissue such as cartilage (Xia 2000).

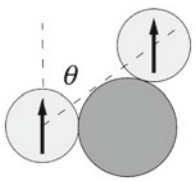

Problem 19. Using Eq. 18.34, determine the value of the minimum correlation time as a function of the Larmor frequency ω_0.
Problem 20. Redraw the plot in Fig. 18.12, assuming protons and your static magnetic field is either 1.5 or 4 T. If the

correlation time is approximately 3 ns, estimate T_1 and T_2. Explain how T_1 and T_2 depend on the magnetic field.

Section 18.7

Problem 21. In solving this problem, you will develop a simple model for estimating the radio-frequency energy absorption in a patient undergoing an MRI procedure.

(a) Consider a uniform conductor with electrical conductivity σ. If it is subject to a changing magnetic field $B_1(t) = B_1 \cos(\omega_0 t)$, apply Eq. 8.21 to a circular path of radius R at right angles to the field to show that the electric field at radius R has amplitude $E_0 = R\omega_0 B_1/2$. (Because this is proportional to R, the model gives the skin dose, along the path for which R is largest.)

(b) Use Ohm's law in the form $j = \sigma E$ to show that the time average power dissipated per unit volume of material is $p = \sigma E_0^2/2 = \sigma R^2 \omega_0^2 B_1^2/8$ and that if the mass density of the material is ρ, the *specific absorption rate* (SAR) or dose rate is $SAR = \sigma R^2 \omega_0^2 B_1^2/8\rho$.

(c) If the radio-frequency signal is not continuous but is pulsed, show that this must be modified by the *duty cycle* factor $\Delta t/T_R$, where Δt is the pulse duration and T_R is the repetition period.

(d) Combine these results with the fact that rotation through an angle θ (usually π or $\pi/2$) in time Δt requires $B_1 = 2\theta/\gamma\Delta t$ and that $\omega_0 = \gamma B_0$, to obtain $SAR = (1/T_R\Delta t)(\sigma/2\rho)R^2 B_0^2 \theta^2$.

(e) Use typical values for the human body—$R = 0.17$ m, $\sigma = 0.3$ S m^{-1}—to evaluate this expression for a $\pi/2$ pulse.

(f) For $B_0 = 0.5$ T and $SAR < 0.4$ W kg^{-1} determine the minimum value of Δt for $T_R = 1$ s. Also find B_1.

(g) For π pulses, what is the dose in Gy? (This should not be compared to an x-ray dose because this is nonionizing radiation.)

Problem 22. Use Eq. 18.38 to calculate the initial amplitude of a signal induced in a one-turn coil of radius 0.5 m for protons in a 1-mm cube of water at 310 K in a magnetic field of 1.0 T. (The answer will be a signal too small to be useful; multiple-turn coils must be used.)

Problem 23. Consider increasing B_0 from 4 T to 7 T. Discuss what changes this will make in

(a) The frequency of the RF pulse,
(b) the signal recorded by the detection coil,
(c) the specific absorption rate (see Problem 21),
(d) the skin depth for magnetic field penetration (see Chap. 8, Problem 29), and
(e) the values of T_1 and T_2.

Section 18.8

Problem 24. Plot the maximum amplitude of an inversion recovery signal vs the interrogation time if the detector is sensitive to the sign of the signal and if it is not.

Problem 25. (a) Obtain an analytic expression for the maximum value of the first and second echo amplitudes in a Carr–Purcell pulse sequence in terms of T_2 and T_E.
(b) Repeat for a CPMG pulse sequence.

Problem 26. Consider the behavior of M_z in Figs. 18.19 and 18.21. The general equation for M_z is $M_z = M_0 + Ae^{-t/T_1}$. After several π pulses, the value of M_z is flipping from $-b$ to b. Find the value of b.

Problem 27. Consider a spin–echo pulse sequence (Fig. 18.18). Find

(a) M_z just before the π pulse at $T_E/2$,
(b) M_z just after the π pulse at $T_E/2$,
(c) M_z just before the $\pi/2$ pulse at T_R, and
(d) the first and second echo amplitudes as a function of T_E, T_R, T_1 and T_2. (The second amplitude is the same as all subsequent amplitudes.)

Problem 28. This problem uses matrices to analyze the spin-echo pulse sequence. Use the rotation matrices given in Problem 12. Start with $\mathbf{M} = (0, 0, M_0)$. Rotate $\mathbf{M}$ about x' by $\pi/2$, then about z' by θ, then about x' by π, and finally about z' by θ. What are the final components of $\mathbf{M}$? Identify what pulse sequence or physical process corresponds to each rotation. Why would θ be nonzero in the rotating reference frame? What would be the significance if the final $\mathbf{M}$ is independent of θ?

Problem 29. (a) Make a three-dimensional sketch of Fig. 18.17. Assume spin a is initially aligned with the y' axis and spin b is 30° clockwise from spin a. Then make similar sketches for a Carr–Purcell sequence that rotates the spins about the x' axis at the following times: just before the π pulse at $T_E/2$, just after the π pulse at $T_E/2$, at T_E, just before the π pulse at $3T_E/2$, just after the π pulse at $3T_E/2$, and at $2T_E$. Assume that the π pulse rotates the spins exactly 180°. Then make sketches when the π pulses rotate the spins by 185°.

(b) Repeat for a CPMG pulse sequence that rotates spin a and spin b around the y' axis. Again, consider two cases: the π pulses rotate by 180° and 185°. Your sketches will show the advantage of the CPMG pulse sequence when there is an error in the duration of the π pulse.

Problem 30. This problem uses the matrices introduced in Problem 12 to examine the difference between the Carr–Purcell and the Carr–Purcell–Meiboom–Gill pulse sequences.

(a) Start with $\mathbf{M} = (0, 0, M_0)$. Rotate about x' by $\pi/2$, about z' by θ, about x' by π, about z' by 2θ, about x' by π, and about z' by θ. What is the final result? This

process corresponds to the first two echoes produced by a Carr–Purcell pulse sequence.

(b) Repeat the analysis of part (a), but change the two π rotations about x' to two $\pi + \delta$ rotations about x'. Assume $\delta \ll \pi$ and use the approximations $\cos(\pi + \delta) = -\cos\delta \approx -1$ and $\sin(\pi + \delta) = -\sin\delta \approx -\delta$ to simplify your result. Keep only terms in order δ. What is your final result? This process corresponds to the first two echoes produced by a Carr–Purcell pulse sequence in which the π pulses have slightly wrong amplitudes.

(c) Repeat the analysis of part (b) but change the rotations about x' to be rotations about y'. What are the differences between the CP and CPMG pulse sequences? Explain why the CPMG pulse sequence is superior to the CP pulse sequence.

Section 18.9

Problem 31. Show that an alternative expression for the field amplitude required for a $\pi/2$ pulse is $B_1 = B_0\pi/\omega_0\Delta t = B_0/2\nu\Delta t$.

Problem 32. A certain MRI machine has a static magnetic field of 1.0 T. Spins are excited while applying a field gradient of 3 mT m^{-1}. If the slice is to be 5 mm thick, what is the Larmor frequency and the spread in frequencies that is required?

Problem 33. Consider a pair of gradient coils of radius a perpendicular to the z axis and located at $z = \pm\sqrt{3}a/2$. The current flows in the opposite direction in each single-turn coil.

(a) Use the results of Problem 8.10 to obtain an expression for B_z along the z axis.

(b) For a gradient of 5 mT m^{-1} at the origin and $a = 10$ cm, find the current required in a single-turn coil.

Problem 34. Find a linear approximation for Eq. 18.53 for very small values of T_E and T_R, and discuss why it is called a T_1-weighted image.

Problem 35. The slice selection gradient G_z must be applied for a time τ which is at least as long as the duration of the B_1 pulse. Suppose that $\tau = 6 \times 2\pi/(\gamma G_z \Delta z)$ (see Fig. 18.23). How much has the phase at the top of the slice ($z = \Delta z$) changed with respect to the middle of the slice ($z = 0$)?

Problem 36. Relate the resolution in the y direction to G_y and T_p.

Problem 37. Discuss the length of time required to obtain a 256×256 image in terms of T_R and T_E. The field of view is 15 cm square. Consider both projection reconstruction and spin warp images. Introduce any other parameters you need.

Problem 38. The limiting noise in a well-designed machine is due to thermal currents in the body. The noise is proportional to B_0 and the volume V_n sampled by the radio-frequency pickup coil. The noise is also proportional to $T^{-1/2}$, where T is the time it takes to acquire the image. Show that the signal-to-noise ratio is proportional to $B_0 T^{1/2} V_v / V_n$, where V_v is the volume of the picture element.

Problem 39. Explain in words why in Fig. 18.24 a negative lobe for G_z to eliminate unwanted phase shifts is not needed following the π pulse, although it is needed following the initial $\pi/2$ pulse.

Problem 40. The readout gradient G_x shown in Fig. 18.26 not only resolves the echo into its frequency components, but also introduces a phase shift. In more detailed analyses the readout gradient consists of two parts: a *prephasing lobe* and a *readout lobe*. Modify Fig. 18.26 to include a prephasing lobe in G_x between the $\pi/2$ and π pulses, so that the net phase shit at the peak of the echo caused by G_x is zero. Pay attention to the amplitude, duration, and polarity of the pulse.

Problem 41. In this book, gradient pulses are drawn as rectangles when showing a pulse sequence. However, there is often a limit, called the *maximum slew rate*, to how fast a gradient can change. Consider a trapezoidal pulse (linear rise, then constant, then linear fall). What is the shortest rise time of the pulse if it has a peak gradient of 30 mT m^{-1} and a maximum slew rate of 100 T m^{-1} s^{-1}?

Problem 42. Suppose one is imaging using the projection reconstruction algorithm shown in Fig. 18.28. After the echo from the initial gradient, when one is ready to repeat the sequence using a different gradient, there may be some residual transverse magnetization that could affect the subsequent signal. Explain why a large G_x gradient, called a *spoiler gradient*, applied after the echo in Fig. 18.28 would eliminate any remaining transverse magnetization.

Section 18.10

Problem 43. The chemical shift difference between water and fat is $\Delta\sigma = 3.5$ ppm. This can cause a spatial shift of the images from fat and water if the readout gradients are large. Estimate this shift for a 1.5 T machine and a gradient of 5 mT m^{-1}.

Section 18.11

Problem 44. Use the model of Sect. 18.11 to plot the flow correction as a function of velocity for $T_E = 10$ ms, $T_1 = 900$ ms, and $T_2 = 400$ ms, when (a) $T_R = 50$ ms, (b) $T_R = 200$ ms.

Problem 45. Excite the spins using a sinc $\pi/2$ pulse and a G_{z1} gradient so that spins in slice $z1$ are in resonance. Then

apply a π pulse, but with a different gradient G_{z2} so the spins are flipped in a different, nonoverlapping slice $z2$.

(a) If the spins are stationary, what signal do you observe?
(b) If the spins move (for instance are carried by flowing blood) from $z1$ to $z2$ during the time between the two RF pulses, what signal do you see?
(c) Design a pulse sequence for performing this experiment.

Problem 46. Suppose your median nerve (the primary nerve in your arm) carries a current I along its length L.

(a) You are having a magnetic resonance image taken, and the steady uniform magnetic field B is directed perpendicular to the nerve. Derive an expression for F, the magnitude of the magnetic force on the nerve. Draw a picture showing the directions of I, **B**, and **F**.
(b) Assume this nerve is held in position by an elastic force per unit length with magnitude equal to kr, where k is the spring constant per unit length and r is the distance the nerve is displaced from its equilibrium position. Find an expression for the displacement of the nerve.
(c) Assume that a magnetic field gradient G is present, so that when the nerve moves a distance r it leaves a region with magnetic field strength B and enters a region of magnetic field strength $B+Gr$. Derive an expression for the change in resonance angular frequency $\Delta\omega$ caused by the displacement, in terms of G, B, I, k, and the gyromagnetic ratio of the proton, γ. (Hint: $\Delta\omega = \gamma\Delta B$). If the gradient and current last for time T, what is the change in phase of the MRI signal?
(d) Calculate the distance that the axon moves if $B_0 = 4$ T, $I = 0.1$ mA, and $k = 40,000$ N m^{-2}. Calculate the resulting phase shift (in degrees) if $G = 36$ mT m^{-1}, $T = 10$ ms, and $\gamma = 2.68 \times 10^8$ rad s^{-1} T^{-1}.

Section 18.13

Problem 47. This problem shows how to extend the Bloch equations to include the effect of diffusion of the molecules containing the nuclear spins in an inhomogeneous external magnetic field. Since **M** is the magnetization per unit volume, it depends on the total number of particles per unit volume with average spin components $\langle\mu_x\rangle$, $\langle\mu_y\rangle$, and $\langle\mu_z\rangle$. In the rotating coordinate system there is no precession. In the absence of relaxation effects $\langle\boldsymbol{\mu}\rangle$ does not change. In that case changes in **M** depend on changes in the concentration of particles with particular components of $\langle\boldsymbol{\mu}\rangle$, so the rate of change of each component of $\langle\boldsymbol{\mu}\rangle$ is given by a diffusion equation. For example, for M_x,

$$\frac{\partial M_{x'}}{\partial t} = D\nabla^2 M_{x'}.$$

If the processes are linear this diffusion term can be added to the other terms in the Bloch equations. Suppose that there is a uniform gradient in B_z, G_z, and that the coordinate system rotates with the Larmor frequency for $z = 0$. When z is not zero, the rotation term does not quite cancel the $(\mathbf{M} \times \mathbf{B})_z$ term.

(a) Show that the x and y Bloch equations become

$$\frac{\partial M_{x'}}{\partial t} = +\gamma G_z z M_{y'} - \frac{M_{x'}}{T_2} + D\nabla^2 M_{x'},$$

$$\frac{\partial M_{y'}}{\partial t} = -\gamma G_z z M_{x'} - \frac{M_{y'}}{T_2} + D\nabla^2 M_{y'}.$$

(b) Show that in the absence of diffusion

$$M_{x'} = M(0)e^{-t/T_2}\cos(\gamma G_z z t),$$

$$M_{y'} = -M(0)e^{-t/T_2}\sin(\gamma G_z z t).$$

(c) Suppose that **M** is uniform in all directions. At $t = 0$ all spins are aligned. Spins that have been rotating faster in the plane at $z + \Delta z$ will diffuse into plane z. Equal numbers of slower spins will diffuse in from plane $z - \Delta z$. Show that this means that the phase of **M** will not change but the amplitude will.
(d) It is reasonable to assume that the amplitude of the diffusion-induced decay will not depend on z as long as we are far from boundaries. Therefore try a solution of the form

$$M_{x'} = M(0)e^{-t/T_2}\cos(\gamma G_z z t)\, A(t),$$

$$M_{y'} = M(0)e^{-t/T_2}\sin(\gamma G_z z t)\, A(t),$$

and show that A must obey the differential equation

$$\frac{1}{A}\frac{dA}{dt} = -D\gamma^2 G_z^2 t^2,$$

which has a solution $A(t) = \exp(-D\gamma^2 G_z^2 t^3/3)$.
(e) Show that if there is a rotation about y' at time $T_E/2$, then at time T_E, M_x is given by

$$M_x(T_E) = -M_0\exp(-T_E/T_2)\exp(-D\gamma^2 G_z^2 T_E^3/12).$$

Hint: This can be done formally from the differential equations. However it is much easier to think physically about the meaning of each factor in the expressions shown in (d) for $M_{x'}$ and $M_{y'}$. This result means that a CPMG sequence with short T_E intervals can reduce the effect of diffusion when there is an external gradient.

Problem 48. A commercial MRI machine is operated with a magnetic gradient of 3 mT m^{-1} while a slice is being selected. What is the effect of diffusion? Use the diffusion

constant for self-diffusion in water and the results of Problem 47. Compare the correction factor to $\exp(-T_E/T_2)$ when $T_2 = 75$ ms.

Problem 49. When a coordinate system is rotated as in Fig. 18.6, the diffusion tensor or diffusion matrix, which is always symmetric, transforms as

$$\begin{pmatrix} D_{x'x'} & D_{x'y'} \\ D_{x'y'} & D_{y'y'} \end{pmatrix} = \begin{pmatrix} \cos\theta & \sin\theta \\ -\sin\theta & \cos\theta \end{pmatrix} \times \begin{pmatrix} D_{xx} & D_{xy} \\ D_{xy} & D_{yy} \end{pmatrix} \begin{pmatrix} \cos\theta & -\sin\theta \\ \sin\theta & \cos\theta \end{pmatrix}.$$

We have not proved this; note that the right-most matrix is the same one that would be seen if Eq. 18.17 were written in matrix form:

$$\begin{pmatrix} M_x \\ M_y \end{pmatrix} = \begin{pmatrix} \cos\theta & -\sin\theta \\ \sin\theta & \cos\theta \end{pmatrix} \begin{pmatrix} M_{x'} \\ M_{y'} \end{pmatrix}.$$

(a) Perform the matrix multiplication and find expressions for $D_{x'x'}$, $D_{x'y'}$, and $D_{y'y'}$ in terms of D_{xx}, D_{xy}, D_{yy}, and θ.

(b) Find the angle θ such that $D_{x'y'}$ is zero (the diffusion tensor is diagonal). This is equivalent to finding the orientation of the fibers in the tissue.

(c) The *trace* of a matrix is the sum of its diagonal elements. Show that the trace of the diffusion matrix in the rotated coordinates, $D_{x'x'} + D_{y'y'}$, is equal to the trace of the diffusion matrix in the original coordinates, $D_{xx} + D_{yy}$. Thus, the trace of the diffusion tensor is independent of fiber direction.

References

Ahrens ET, Zhong J (2013) In vivo MRI cell tracking using perfluorocarbon probes and fluorine-19 detection. NMR Biomed 26: 860–871. doi:10.1002/nbm.2948

Axel L (1984) Blood flow effects in magnetic resonance imaging. Am J Roentgenol 143:1157–1166

Bandettini PA, Petridou N, Bodurka J (2005) Direct detection of neuronal activity with MRI: fantasy, possibility, or reality? Appl Magn Reson 29:65–88

Basser PJ, Mattiello J, LeBihan D (1994) MR diffusion tensor spectroscopy and imaging. Biophys J 66:259–267

Basser PJ, Pajevic S, Pierpaoli C, Duda J, Aldroubi A (2000) In vivo fiber tractography using DT-MRI data. Magn Reson Med 44: 625–632

Battocletti JH, Halbach RE, Salles-Cunha SX (1981) The NMR blood flow meter—theory and history. Med Phys 8:435–443

Bernstein MA, King KF, Joe Zhou X-h (2004). Handbook of MRI pulse sequences. Elsevier Academic Press, Amsterdam

Brown RW, Cheng Y-CN, Haacke EM, Thompson MR, Venkatesan R (2014) Magnetic resonance imaging: physical properties and sequence design. Wiley-Blackwell, Hoboken

Callaghan P (1994) Principles of nuclear magnetic resonance microscopy. Oxford University Press, Oxford

Chen W, Kato T, Zhu X-H, Strupp J, Ogawa S, Ugurbil K (1998) Mapping of lateral geniculate nucleus activation during visual stimulation in the human brain using fMRI. Magn Reson Med 39(1):89–96

Cho Z-H, Jones JP, Singh M (1993) Foundations of medical imaging. Wiley-Interscience, New York

Delannoy J, Chen CN, Turner R, Levin RL, LeBihan D (1991) Noninvasive temperature imaging using diffusion MRI. Magn Reson Med 19:333–339

Hao D, Ai T, Goerner F, Hu X, Runge VM, Tweedle M (2012) MRI contrast agents: Basic chemistry and safety. J Mag Res Imaging 36:1060–1071. doi:10:1002/jmri.23725

Harisinghani MG, Barentsz J, Hahn PF, Deserno WM, Tabatabaei S, van de Kaa CH, de la Rosette J, Weissleder R (2003) Noninvasive detection of clinically occult lymph-node metastases in prostate cancer. N Engl J Med 348(25):2491–2499

Joseph PM, Axel L, O'Donnell M (1984) Potential problems with selective pulses in NMR imaging systems. Med Phys 11(6):772–777

Kanal E et al (2007) ACR guidance document for safe MR practices: 2007. Am J Roentgenol 188:1447–1474. doi:10.2214/AJR.06.1616

Kim BH et al (2011) Large-scale synthesis of uniform and extremely small-sized iron oxide nanoparticles for high resolution T_1 magnetic resonance imaging contrast agents. J Am Chem Soc 133:12624–12631

Koh D-M, Cook GJR, Husband JE (2003) New horizons in oncologic imaging. N Engl J Med 348(25):2487–2488

Kwong KK, Belliveau JW, Chesler DA, Goldberg IE, Weisskoff RM, Poncelet BP, Kennedy DN, Hoppel BE, Cohen MS, Turner R, Cheng HM, Brady TJ, Rosen BR (1992) Dynamic magnetic resonance imaging of human brain activity during primary sensory stimulation. Proc Nat Acad Sci U S A 89(12):5675–5679. doi:10.1073/pnas.89.12.5675

Lei H, Zhu X-H, Zhang X-L, Ugurbil K (2003) In vivo ^{31}P magnetic resonance spectroscopy of the human brain at 7 T: an initial experience. Magn Reson Med 49:199–205

Levitt MH (2008) Spin dynamics, 2nd edn. Wiley, New York

Liang Z-P, Lauterbur PC (2000) Principles of magnetic resonance imaging: a signal processing perspective. IEEE Press, New York

Louie A (2013) MRI biosensors: a short primer. J Mag Res Imaging 38:530–539. doi:10.1002/jmri.24298

Mariappan YK, Glaser KJ, Ehman RL (2010). Magnetic resonance elastography: a review. Clin Anat 23:497–511

Mattiello J, Basser PJ, LeBihan D (1994) Analytical expressions for the B-matrix in NMR diffusion imaging and spectroscopy. J Magn Reson Ser A 108:131–141

Moseley ME, Cohen Y, Mintorovitch J, Chileuitt L, Shimizu H, Kucharczyk J, Wendland MF, Weinstein PR (1990) Early detection of regional cerebral ischemia in cats: comparison of diffusion- and T_2-weighted MRI and spectroscopy. Magn Reson Med 14:330–346

Mugler JP, Altes TA (2013) Hyperpolarized ^{129}Xe MRI of the human lung. J Magn Reson Imag 37:313–331

Ogawa S, Lee TM, Kay AR, Tank DW (1990) Brain magnetic resonance imaging with contrast dependent on blood oxygenation. Proc Natl Acad Sci U S A 87:9868–9872

Robitaille P-M, Berliner LJ (2006) Ultra high field magnetic resonance imaging. Springer, New York

Sakuma H (2007) Magnetic resonance imaging for ischemic heart disease. J Magn Reson Imaging 26:3–13

Santini L, Forelo GB, Santini M (2013) Evaluating MRI-compatible pacemakers: patient data now paves the way to widespread clinical application? PACE 36:270–278. doi:10.1111/pace.12061

Schaefer DJ, Bourland JD, Nyenhuis JA (2000) Review of patient safety in time-varying gradient fields. J Magn Reson Imaging 12:20–29

Schmitt F, Stehling MK, Turner R (1998). Echo-planar imaging. Springer, Berlin

Slichter CP (1990) Principles of magnetic resonance, 3rd edn. Springer, New York

Thomas DL, Lythgoe MF, Pell GS, Calamante F, Ordidge RJ (2000) The measurement of diffusion and perfusion in biological systems using magnetic resonance imaging. Phys Med Biol 45:R97–R138

Vlaardingerbroek MT, den Boer JA (2004) Magnetic resonance imaging: Theory and practice, 3rd edn. Springer, Berlin

Wolf RL, Detre JA (2007) Clinical neuroimaging using arterial spin-labeled perfusion magnetic resonance imaging. Neurotherapeutics 4:346–359

Xia Y (2000) Magic angle effect in magnetic resonance imaging of articular cartilage: a review. Invest Radiol 35:602–621